

RESEARCH ARTICLE

10.1029/2018JB016350

Key Points:

- A strong velocity contrast associated with the western Idaho shear zone is visible to midcrustal depths
- The Greenhorn subterrane overthrusts the Bourne subterrane during or after accretion to North America
- Shortening and thickening of plutonic complexes may have formed thick felsic crust in the Blue Mountains terranes

Correspondence to:

P. M. Bremner,
pbremner@ufl.edu

Citation:







Bremner, P. M., Panning, M. P., Russo, R. M., Mocanu, V., Stanciu, A. C., Torpey, M., et al. (2019). Crustal shear wave velocity structure of central Idaho and eastern Oregon from ambient seismic noise: Results from the IDOR project. *Journal of Geophysical Research: Solid Earth*, 124. <https://doi.org/10.1029/2018JB016350>

Received 16 JUL 2018

Accepted 28 DEC 2018

Accepted article online 2 JAN 2019

Crustal Shear Wave Velocity Structure of Central Idaho and Eastern Oregon From Ambient Seismic Noise: Results From the IDOR Project

Paul M. Bremner¹ , Mark P. Panning^{1,2} , R. M. Russo¹ , Victor Mocanu³, A. Christian Stanciu^{1,4} , Megan Torpey^{1,5}, Sutatcha Hongsresawat^{1,6}, John C. VanDecar⁷ , Todd A. LaMaskin⁸, and D. A. Foster¹ 

¹Department of Geological Sciences, University of Florida, Gainesville, FL, USA, ²Now at Jet Propulsion Laboratory, California Institute of Technology, Pasadena, CA, USA, ³Department of Geology and Geophysics, University of Bucharest, Bucharest, Romania, ⁴Now at Earth Sciences Department, University of Oregon, Eugene, OR, USA, ⁵Now at AIR Worldwide, Boston, MA, USA, ⁶Now at Division of Geoscience, Mahidol University, Kanchanaburi, Thailand, ⁷DTM-Carnegie Institution of Washington, Washington, DC, USA, ⁸Department of Geography and Geology, University of North Carolina at Wilmington, Wilmington, NC, USA

Abstract We developed 3-D isotropic crustal seismic velocity models of central Idaho and eastern Oregon from the IDOR (western Idaho and eastern Oregon) Passive seismic data. Ambient noise tomography yielded crustal velocity structure from vertical component Rayleigh wave group and phase velocity measurements. Results include a strong shear wave velocity contrast—faster in accreted Blue Mountains terranes west of the western Idaho shear zone (WISZ), slower in the Idaho batholith, emplaced within the Archean Grouse Creek block east of the WISZ—restricted to the upper-to-middle crust. In deeper crust not affected by mafic underplating during Columbia River Flood Basalt magmatism, the shear wave velocity of the Mesozoic Olds Ferry continental arc terrane is indistinguishable from that of the Archean Grouse Creek block basement. Crustal columns of the Olds Ferry terrane and the Permian-Jurassic Wallowa intraoceanic arc terrane are characterized by low seismic velocities, consistent with felsic lithologies down to ~20 km. West of the WISZ, the Bourne and Greenhorn subterranes of the Baker terrane, an accretionary complex between the arc terranes, have distinct shallow crustal seismic velocities. The Greenhorn subterrane to midcrustal depths is in an overthrust geometry relative to the Bourne subterrane. Lack of mafic lower crust in our results of the Wallowa or Olds Ferry arcs may be due to imbrication of upper crustal felsic plutonic complexes of these arcs. Shortening and thickening of the Blue Mountains arc terranes crust to >30 km, and subduction or delamination of their mafic lower crustal sections is a viable mechanism for growth of a felsic continental crust.

1. Introduction

Ambient seismic noise tomography (ANT) is a powerful tool for measuring high-quality lithospheric velocity dispersion curves over regional to continental scales (e.g., Bensen et al., 2007; Gallego et al., 2010; Lin et al., 2008; Shapiro et al., 2005). The method entails calculation of an estimated Green's function between two seismic stations, derived from stacking many long, cross-correlated time series of seismic “noise” recorded simultaneously at seismic stations (e.g., Gerstoft et al., 2006; Lobkis & Weaver, 2001; Shapiro & Campillo, 2004). The recovered Green's function is comparable to those from ballistic seismic wave analyses and contains valuable information of Earth's structure along the path between the station pair. When used with data from a closely spaced network of stations, ANT yields a greater azimuthal distribution of sources and higher resolution than that achievable in many teleseismic studies. ANT is particularly well suited for probing the crust and uppermost mantle, due to a higher frequency content than typically observed from teleseismics, and has been successfully employed in a variety of tectonic settings (e.g., Gallego et al., 2010; Lin et al., 2008; Shapiro et al., 2005; Yang et al., 2011).

This study is part of the multidisciplinary Earthscope IDOR (western Idaho and eastern Oregon) project, which had an overarching goal of determining the tectonic history of western Idaho and eastern Oregon, and specifically the formation and evolution of the steep accretionary boundary associated with the Salmon

River suture zone and western Idaho shear zone (WISZ; Tikoff et al., 2017). As a part of the IDOR project, both passive and controlled-source seismic experiments were conducted to determine the current geometry of major geologic units and crustal thickness. To distinguish our effort from other components of the IDOR project, we refer to the passive component of the IDOR project as IDOR Passive. The IDOR Passive seismic network entailed 85 broadband three-component CMG-3T Guralp seismometers deployed between May 2011 and June 2013. Figure 1 shows the geographic location of the stations within context of major geologic boundaries. The network consisted of a dense ~E-W trending line of 29 stations spaced ~15 km apart (hereafter referred to as the L-line), plus 56 stations distributed north and south of the L-line, spaced ~35 km apart. The L-line stations were approximately collocated with the line of IDOR controlled-source seismophones, deployed in August 2012 (Davenport et al., 2017).

In this study, we used ANT to determine the isotropic 3-D crustal shear velocity structure of the IDOR study region to infer the geometry of the region's crustal geologic units. We processed nearly 2 years of vertical component seismic data from the IDOR Passive seismic network, plus two permanent broadband stations: Hailey, Idaho (HLID) and Blue Mountain Observatory in Oregon (BMO; Figure 1). In the following, we review the geologic setting and the makeup of major geologic provinces of the study area. This review of the crustal geology is necessary to place our results in proper context. Next, we outline the methods used to obtain group and phase velocity maps, which we then used to produce the 3-D velocity structure. We then present a new 3-D isotropic crustal shear wave velocity structure of the study area, as well as associated resolution tests, and discuss tectonic implications.

2. Tectonic Setting

To first order, the study area can be divided into two major geologic provinces lying east and west of the WISZ, a subvertical strike-slip fault zone that juxtaposes Precambrian North America, to the east, and Late Paleozoic to Jurassic island arc terranes and associated subduction complexes of the Blue Mountains Province (BMP) to the west (e.g., Davenport et al., 2017; Gaschnig et al., 2011; LaMaskin et al., 2015; Lund & Sneek, 1988; Tikoff et al., 2001; Stanciu et al., 2016; Wyld & Wright, 2001; see Figure 1). The arc terranes of the BMP accreted to North America before Late Jurassic time (LaMaskin et al., 2015) and are today structurally imbricated with rocks of the Salmon River Belt (Gray & Oldow, 2005; LaMaskin & Dorsey, 2016; McKay et al., 2017) preserved at the surface to the north of the IDOR Passive seismic deployment. The Salmon River Belt at the latitudes of our project was later modified by the narrow (currently ~5 km in width), north-striking zone of dextral transpression of the WISZ, active roughly between 125 and 90 Ma (Gaschnig et al., 2011; McKay et al., 2017; Tikoff et al., 2001; Wyld & Wright, 2001). The Blue Mountains terranes translated north along the WISZ during its activity to their current location; estimates of the displacement entailed vary from ~80 km (Giorgis et al., 2008) to ~400 km (LaMaskin et al., 2011; Wyld & Wright, 2001), based on tectonic reconstructions, although paleomagnetic analyses indicate ~1,700 km of northward translation (Housen & Dorsey, 2005). Subduction beneath North America continued following the Blue Mountains accretion and translation, culminating in the Late Mesozoic-early Cenozoic Sevier-Laramide shortening of the Northern Rockies. During this subduction, the Idaho batholith (IB) developed on North American basement to the east of the WISZ, on Precambrian basement of the Grouse Creek and Selway terranes (Foster et al., 2006; Gaschnig et al., 2010, 2011). Waning subduction was accompanied by eruption of the Challis volcanics and Eocene extension in central and eastern Idaho (Lewis & Kiilsgaard, 1991). The most recent tectonism to affect the study area includes, apparently, passage over the distal portions of the Yellowstone hotspot swell, Miocene-present Basin and Range extension (Payne et al., 2012; Vogl et al., 2014), and—west of the WISZ—the Blue Mountains terranes are extensively covered by Miocene Columbia River Flood Basalts (Reidel et al., 2013).

2.1. North American Precambrian Basement

The discernible Phanerozoic history of the study area began with formation of a rifted passive margin along western Laurentia during Neoproterozoic-Cambrian time (Bond et al., 1984; Colpron et al., 2002; Lund, 2008; Stewart, 1972); this passive margin endured until the Devonian (Lund, 2008; Pyle & Barnes, 2003). The Precambrian basement east of the WISZ consists of an assemblage of Proterozoic and Archean terranes (Foster et al., 2006; Gaschnig et al., 2013; Hoffman, 1988; Karlstron et al., 2002; Mueller et al., 2011; Ross, 1991; Sims et al., 2005), including the Selway and Grouse Creek basement blocks and the western part of the Wyoming craton (Figure 1, e.g., Foster et al., 2006; Mueller et al., 2011; Sims et al., 2005).

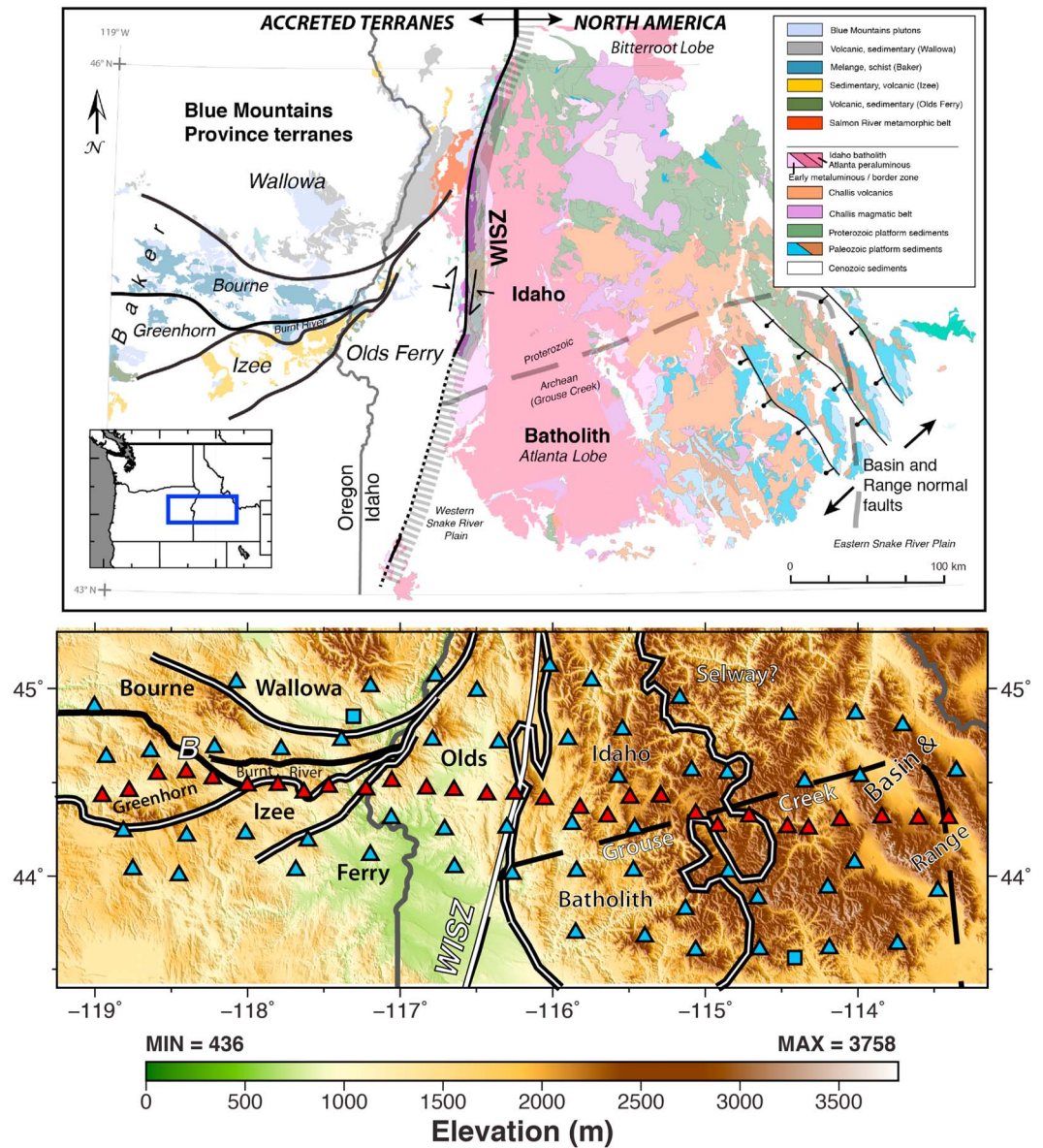


Figure 1. (top) Location and simplified geologic setting of the IDOR (western IDAHO and eastern OREGON) Passive seismic project study area. Western Idaho shear zone (WISZ) (Gaschnig et al., 2011) divides Blue Mountains Province to the west from Precambrian North America to the east (modified from Davenport et al., 2017, Figure 1). Major lithologic and sedimentary units color coded according to legend. (inset map) Geographic context. Blue box indicates IDOR study area shown in bottom panel. (bottom) Triangles denote locations of the 85 IDOR broadband seismic stations and two permanent broadband stations, Hailey, Idaho and Blue Mountain Observatory in Oregon (light blue squares), used in this study. Red triangles are the L-line stations lying along the IDOR controlled-source seismic project geophone line; light blue triangles denote all other IDOR Passive stations (see text for more detail). (white lines) Major terrane/province boundaries and WISZ. (thick dashed black line) Northern and eastern boundary of the Grouse Creek basement block; solid black lines are subterranean boundaries within the Baker terrane (B). Terrane boundaries within the Blue Mountain province from LaMaskin et al. (2015).

Paleoproterozoic basement of the Selway terrane, comprising predominantly 1.6- to 2.4-Ga-age metamorphic and igneous rocks (Foster et al., 2006) with some remnant Precambrian sedimentary cover of the Belt (Lemhi; 1470–1380 Ma) and Windermere (<850–600 Ma) Supergroups, underlies the northeastern part of the study area (Figure 1). The Belt units are intracratonic rift deposits, and the Windermere rocks were deposited within rifts and on the rifted continental margin (e.g., Lund et al., 2003; Price & Sears, 2000; Ross, 1991; Stewart, 1972; Winston & Link, 1993). The Archean Grouse Creek block (Figure 1; Foster et al., 2006;

Gaschnig et al., 2013) lies south of the Selway terrane and constitutes the majority of the Laurentia basement on which our seismic stations were deployed (Stanciu et al., 2016). Belt and Windermere units also partly cover the Grouse Creek block in the eastern portion of our study area. East of the Selway and Grouse Creek terranes, the Archean Wyoming craton (e.g., Foster et al., 2006; Mueller et al., 2011; Sims et al., 2005) is distinct due to its thick crust and high seismic velocities relative to the adjacent Proterozoic terranes (Henstock et al., 1998). The boundaries between the Selway terrane, Grouse Creek block, and Wyoming craton are poorly defined and of unclear tectonic character. The Selway-Grouse Creek boundary is entirely cryptic but implied by the occurrence of 2.55- to 2.65-Ga-age zircons within only the southern Late Cretaceous Atlanta lobe of the IB (Gaschnig et al., 2013). South of the IDOR Passive deployment footprint, in Utah, the Farmington zone separates the Wyoming craton and the Archean Grouse Creek block (Figure 1; Foster et al., 2006; Mueller et al., 2011). The extension of this zone north into Idaho and SW Montana is consistent with exposures of similar aged rocks in SW Montana (~2.4 Ga; Foster et al., 2006), and with a clear Moho offset within the IDOR footprint that is coincident with the presumed surface trace of the Farmington zone (Stanciu et al., 2016).

2.2. Idaho Batholith

Immediately east of the WISZ, the granitic rocks of the IB intruded Selway and Grouse Creek basement and the Proterozoic-Paleozoic cover rocks. Current exposures of the southern parts of the batholith were emplaced at shallow to midcrustal depths (Fayon et al., 2017). Figure 1 shows the two major lobes of the batholith: the Bitterroot lobe to the north and the larger Atlanta lobe to the south. Of these, the IDOR Passive seismic network was deployed on the Atlanta lobe. Gaschnig et al., 2010 (2010, 2011) identified three distinct magmatic suites that make up the Atlanta lobe, based on bulk-rock lithology. The first two suites, the early metaluminous and border zone suites, were emplaced between 98 and 87 Ma and about 90 Ma, respectively. They had a hybrid crust-mantle source and are present just east of the WISZ and along the outlying perimeter of the Atlanta lobe. The Atlanta lobe peraluminous suite, the majority of surface exposures, was emplaced between 83 and 67 Ma and is the result of melting of continental material due to crustal thickening (Gaschnig et al., 2010, 2011). Both IB lobes are part of a much larger suite of Mesozoic batholiths outcropping virtually ubiquitously along strike of the North American Cordillera but whose longitudinal position varies significantly: North of 50° N and south of 32° N, the batholiths currently occupy near-coastal locations; however, the IB lies anomalously some 500 km to the east of the west coast of North America. The anomalous location of the IB and its development largely from melting of continental material are consistent with its formation as part of a large Cordilleran plateau similar to the Andean Altiplano (Coney & Harms, 1984; Fayon et al., 2017; Foster et al., 2001; Gaschnig et al., 2013; Jordan & Allmendinger, 1986; Miller & Bradfish, 1980; Russo & Silver, 1996; Sewall & Fricke, 2013).

The Challis volcanic field both intruded and was extruded upon east and central Idaho between 51 and 44 Ma and overprints eastern portions of the Atlanta lobe of the IB (Gaschnig et al., 2011). The Challis volcanics are associated with the Kamloops-Challis-Absaroka volcanic episode that affected an area from southern Idaho northward to Alaska (Armstrong & Ward, 1991) and show both crust-mantle hybrid and crustal sources (Gaschnig et al., 2011). This volcanism coincided with the onset of early Eocene extension east of the IB, beginning by 53 ± 1 Ma (Foster & Fanning, 1997; Foster et al., 2007, 2010).

2.3. Blue Mountains Province Terranes

Accreted terranes of the BMP outcrop west of the WISZ (Kurz et al., 2017; Lallemand, 1995; LaMaskin et al., 2015; Schwartz et al., 2011). These arc terranes formed as intraoceanic and fringing arc systems along the western coast of Laurentia between Permian and Jurassic time, and they accreted to the western margin of North America before Late Jurassic (Gray & Oldow, 2005; Kurz et al., 2017; LaMaskin et al., 2015; Figure 1). Rocks of the BMP are juxtaposed against the Salmon River Belt, a zone of east-dipping, west-verging metamorphic rocks outcropping in west-central Idaho and easternmost Oregon, which have been interpreted as the subduction-related structure along which the Blue Mountains terranes accreted (Gray & Oldow, 2005; Lund & Snee, 1988; McKay et al., 2017; Selverstone et al., 1992; Strayer et al., 1989; Schwartz et al., 2010). Alternatively, LaMaskin et al. (2015) and LaMaskin and Dorsey (2016) have suggested that the Salmon River Belt is a Cretaceous thrust belt associated with Sevier deformation along the western U.S. plate margin. These authors suggest that the Blue Mountains terranes accreted in Middle Jurassic time at the latitude of Nevada and that deformation in the WISZ has obscured original accretion relationships. The BMP includes two distinct crystalline basement terranes, the Wallowa and Olds Ferry island arc terranes; the Baker terrane, a metamorphosed accretionary complex that formed between the two arcs; and the sedimentary cover

units of the Izee terrane (e.g., Dickinson, 2004; Dorsey & LaMaskin, 2007; LaMaskin et al., 2015; Schwartz et al., 2010). After amalgamation to North America, the BMP underwent dextral-transpressive displacement northward along the North American margin. We describe these units in more detail in the following, in order to provide context for interpretations in the section 5, below.

2.3.1. Olds Ferry Island Arc Terrane

The Olds Ferry island arc terrane is the most inboard (continentward) of the Blue Mountains terranes and is composed of a wide compositional range of arc rocks, from basalts to rhyolites—but predominantly andesites—and volcanigenic sediments and sedimentary rocks of Middle Triassic to Lower Jurassic ages. Geochronology of appropriate units within the Olds Ferry and overlying Izee terranes indicate that it functioned as an active arc—with hiatuses—from 238–210 Ma (Kurz et al., 2017). Zircons in the sediments indicate a clear contribution from continental North America, which either was basement to the Olds Ferry arc, or must have been nearby during the Olds Ferry activity. In addition, Olds Ferry rocks are isotopically distinct from those of the Wallowa terrane and include continent-derived material, indicating that the arc may have developed on the western margin North America (Kurz et al., 2017). During and subsequent to its displacement with respect to stable North America, the Olds Ferry was metamorphosed to greenschist facies (e.g., Gray & Oldow, 2005; Kurz et al., 2017; LaMaskin et al., 2008; Schwartz et al., 2011; Tumpene, 2010). The Olds Ferry terrane underlies the southwesternmost portion of the IDOR study area (Figure 1). It outcrops rarely but is exposed along the Snake River on the west side of Hells Canyon.

2.3.2. Wallowa Island Arc Terrane

The Wallowa terrane is a Permian-Early Jurassic composite intraoceanic island arc terrane (e.g., Gray & Oldow, 2005; Kurz et al., 2017; LaMaskin et al., 2008, 2015; Schwartz et al., 2011). Plutonic basement rocks of the Wallowa crystallized ~264–215 Ma and were intruded and/or overlain by Early Triassic to Early Cretaceous sedimentary and volcanic rocks, including granitic rocks of the Early Cretaceous Wallowa batholith (e.g., Schwartz et al., 2011). Arc magmatism persisted, also with hiatuses, from 263–229 Ma (Kurz et al., 2017). Unlike the Olds Ferry arc, the Wallowa arc did not develop within range of isotopic contributions from North America during its active phase (Kurz et al., 2017). The Wallowa terrane outcrops in the northwesternmost part of the IDOR Passive seismic network footprint.

2.3.3. Baker Terrane

The Baker terrane formed as an accretionary complex between the Wallowa and Olds Ferry terranes (Ferns & Brooks, 1995; Schwartz et al., 2010). It is an Early Permian to Early Jurassic mix of nonarc ocean-floor basalts, island arc volcanic and plutonic rocks, and sedimentary rocks. Vergence of remnant structures within the Baker terrane indicate that it occupied a forearc position adjacent to the Olds Ferry side of the bivergent Olds Ferry-Wallowa subduction system (e.g., Dorsey & LaMaskin, 2007; Gray & Oldow, 2005; Schwartz et al., 2010). The Baker terrane is divided into three subterrane: the Bourne, the Greenhorn, and Burnt River Schist subterrane. Brittle to semibrittle deformation related to BMP amalgamation is localized along sporadically outcropping south-dipping tectonic contacts between the Wallowa and the Bourne (Schwartz et al., 2010), the Bourne and Greenhorn, and the Greenhorn and Olds Ferry terranes (Schwartz et al., 2011).

The Bourne subterrane outcrops directly south of the Wallowa terrane and is an accretionary complex (Ferns & Brooks, 1995; Schwartz et al., 2010) dominantly consisting in exposures of deformed chert beds and argillites (Schwartz et al., 2011). Southward-dipping moderate to low-angle reverse and thrust fault-bounded slabs of arc-related plutons and volcanoclastic rocks also occur in the Bourne subterrane near the Wallowa boundary and have been interpreted as imbricated fragments of Wallowa rocks intercalated into the Bourne subterrane after the Late Triassic (Schwartz et al., 2011). Pillow basalts and associated volcanoclastic and metasedimentary rocks are present near the Bourne-Greenhorn boundary and are geochemically distinct from the arc-related rocks near the Wallowa boundary (Schwartz et al., 2011). Devonian McCloud (North American affinity) and Tethyan (offshore) affinity microfossils have been found in limestones of the Bourne subterrane (Schwartz et al., 2011).

The Greenhorn subterrane outcrops south of the Bourne subterrane and is identified as the forearc of the Olds Ferry island arc system (Schwartz et al., 2011). The Greenhorn subterrane largely consists of serpentinite-matrix mélange and large blocks of arc-related metaplutonic and metavolcanic rocks. These are overlain by Permian-Triassic conglomerate and metasedimentary rocks (Schwartz et al., 2011). Unlike the Bourne subterrane, the Greenhorn only contains McCloud affinity microfossils (Mullen, 1978; Schwartz et al., 2011).

The Burnt River Schist subterrane is thought to be a portion of accretionary complex similar to the Bourne subterrane (Ashley, 1995) but isotopically distinct from it (Schwartz et al., 2011). It consists of a heterogeneous mix of mostly fine-grained metasediments and also includes marbles and metavolcanic and mafic-felsic metaplutonic rocks (Ashley, 1995; Schwartz et al., 2011).

The Izee terrane is a variably thick (up to 15 km) succession of Triassic to Jurassic sedimentary strata, which overlies the Olds Ferry arc on a faulted unconformity (Dorsey & LaMaskin, 2007; LaMaskin et al., 2015). The Izee was initially thought to be solely a forearc basin succession (e.g., Dickinson, 1979; Gray & Oldow, 2005) but more recently Middle Jurassic portions have been interpreted as a collisional overlap succession (Dorsey & LaMaskin, 2007).

The BMP units and areas of southern Idaho have been strongly affected by Miocene-present Basin and Range extensional deformation (e.g., Payne et al., 2012). The BMP is also the locus of prolific eruptions of the Columbia River flood basalts, beginning ~ 17 Ma. The latter now cover a large portion of the IDOR Passive seismic network footprint in central Oregon and western Idaho (Reidel et al., 2013). Discernible effects of the genesis of the Columbia River flood basalts may include a modest increase in lower crustal P -wave seismic velocities beneath the BMP terranes (Davenport et al., 2017).

3. Methodology

3.1. Cross Correlations

The raw vertical component seismic data of displacements (from 2011 to 2013) were corrected for instrument response, band-pass filtered between 2- and 30-s periods, downsampled to two samples per second, and we removed the mean and trend (Gallego et al., 2010). We then cross-correlated 24-hr segments of vertical component binary seismograms for every pair of stations and stacked all cross-correlograms of each station pair. Figure 2 shows a record section plot of the stacked cross-correlograms for the L-line station pairs (red triangles in Figure 1), all referenced to the westernmost station (L29). The dominant peak amplitudes, which progressively move out with increasing interstation distance define a west-to-east propagating Rayleigh wave with a velocity of ~ 3 km/s. The causal time direction Rayleigh wave amplitudes are greater than those of the acausal direction, reflecting a stronger signal source from the west. The symmetric empirical Green's functions (EGFs) were calculated by averaging the causal and acausal stacked cross-correlogram directions for each station pair to reduce source distribution inhomogeneity effects, then taking the derivative with respect to time to change from displacements to velocities, and changing sign to adjust the phase of the cross-correlograms (Lin et al., 2008, equation 5):

$$G_{AB}(t) = -\frac{d}{dt} \left[\frac{C_{AB}(t) + C_{AB}(-t)}{2} \right] \quad 0 \leq t < \infty, \quad (1)$$

where G_{AB} is the symmetric EGF and $C_{AB}(t)$ and $C_{AB}(-t)$ are the positive and negative cross-correlogram directions, respectively. Finally, it is desirable to measure traveltimes in many narrow frequency bands to calculate more accurate dispersion curves. The trade-off, however, is that temporal resolution decreases (the signal envelope widens) as frequency bandwidth decreases. This increases measurement error, and for short traveltimes we observed that the envelope from the positive and negative sides of the EGF's merged, leading to apparent near-zero traveltimes.

Multiplying by the Heaviside step function prior to filtering eliminated the influence of the acausal side of the EGF on the shape of the signal envelope on the positive side. In this way, we converted all EGFs to one-sided EGFs to allow traveltime measurements in narrow frequency bands, with a width in period $\pm 10\%$ seconds around a central period. We divided the overall bandwidth of 2- to 30-s period into 25 overlapping bands, 24 of which produced reliable traveltime measurements and 14 of which were utilized in the 2-D group and phase velocity maps.

3.2. Group Velocity Measurements

We made frequency-dependent interstation velocity measurements for two independent observables, group and phase velocities. The group velocity was measured first, and a network averaged group velocity profile was constructed. The initial phase velocity profile was estimated from this network average. To measure the group velocity dispersions, we first estimated the Rayleigh wave wavelength (λ) at the central period in each

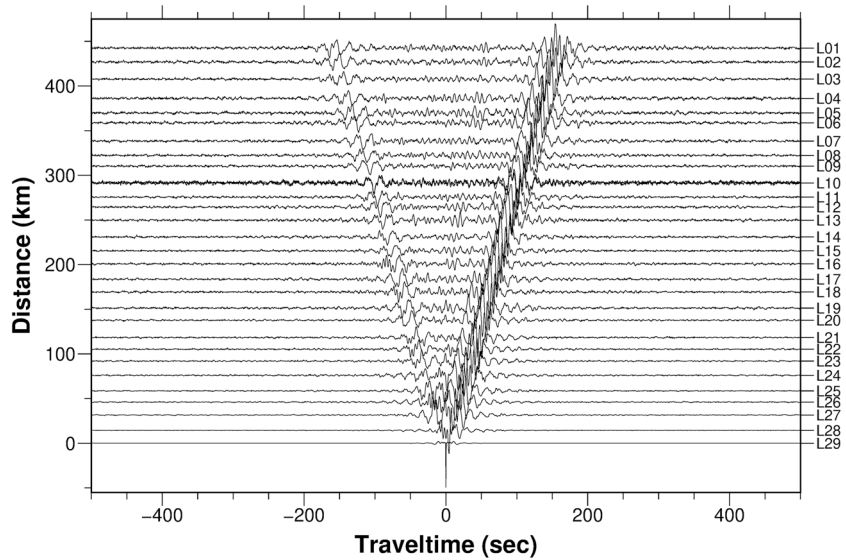


Figure 2. Record section plot of vertical component stacked cross-correlograms for the L-line station pairs showing a well-defined Rayleigh wave propagating at ~ 3 km/s. All station pairs are referenced to L29, the westernmost L-line station. Positive y direction is increasing interstation distance from west to east, and x axis is traveltime of seismic energy from the reference station to the second station.

of the 25 frequency bands by initially assuming a velocity of 2 km/s. All data with interstation distances less than $1.5 \times \lambda$ were excluded. In each frequency band, we took the envelope of the one-sided EGFs and measured the traveltime to the highest peak amplitude for all remaining data. The signal-to-noise ratio (SNR) was found by taking the root mean square of ± 25 s about the traveltime divided by the root mean square of the last 100 s of the one-sided EGF (Gallego et al., 2010).

3.2.1. Data Winnowing

In some cases, the procedure described above produced unrealistically high or low velocities. We filtered the data to remove spurious velocity estimates and retained only high-quality measurements as input to the inversion for earth structure. Thus, we removed all data with SNR less than 6, as well as all obviously spurious velocity measurements outside the range 0.5–5 km/s. Finally, we determined the network averaged group velocity dispersion curve by averaging all individual station pair path-averaged velocities at each period and calculated the corresponding standard deviation (σ). We discarded data beyond 3σ from the network mean to remove outlying measurements. The resulting group velocity dispersion curve is shown in Figure 3, and Figure 4 shows the final count of retained measurements as a function of azimuth for each period.

3.2.2. Two-Dimensional Group Velocity Maps

We calculated 2-D velocity models for each period using a damped least squares inversion from the path-averaged group velocity measurements (Tarantola, 2005). We used a linear inversion scheme that inverted for damped, absolute slowness as

$$M = M_0 + [G^T C_D^{-1} G + (C_M^{-1} + \epsilon I)]^{-1} G^T C_D^{-1} (d_{\text{obs}} - G M_0), \quad (2)$$

where M_0 is the initial model vector (slowness), M is the new estimated model vector, G is the kernel matrix containing information about path geometry, G^T is the transpose of G , C_D is the data covariance matrix, C_M is model covariance matrix, and d_{obs} is a vector containing traveltimes. The data covariance matrix, C_D , is a diagonal matrix where each element has an allowed 1.0-s traveltime measurement error plus a coefficient that

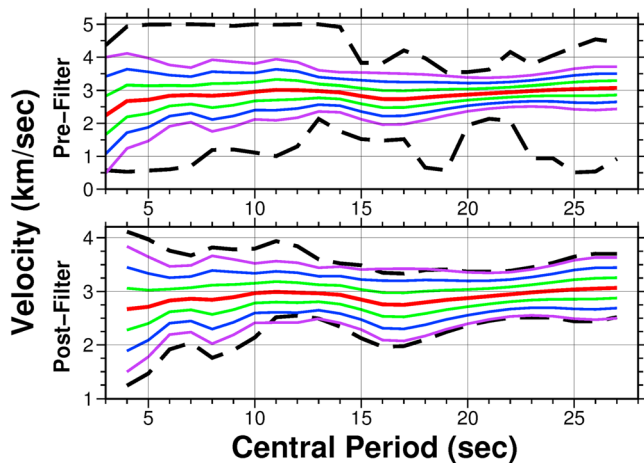


Figure 3. Vertical component network averaged group velocity dispersion curves. The top panel shows velocity dispersion after filtering out data with SNR < 6 , and apparent velocities above 5 km/s and below 0.5 km/s. The bottom panel shows velocity dispersion after filtering data from the top panel to $\pm 3\sigma$. The red lines show mean velocity; green, blue, and purple lines show the ± 1 , 2, and 3σ deviations, respectively; and the black dashed lines show the min/max velocities.

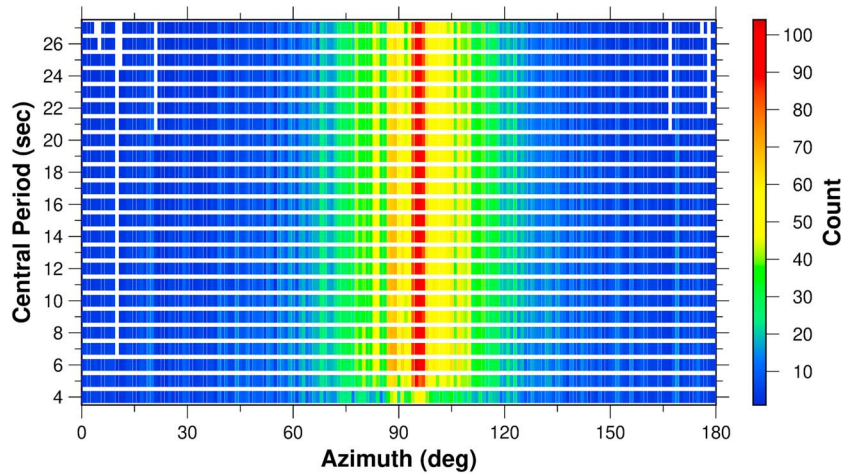


Figure 4. Number of vertical component group velocity measurements as a function of azimuth for each period. The 0° – 180° and 180° – 360° azimuths were summed as they are equivalent for the symmetric empirical Green’s functions. Note that the seismic network geometry results in a large number of east-west paths producing an azimuthal bias.

scales with the SNR of each measurement (SNR_i), or

$$C_{D,ii} = \frac{1.0}{\left(1.0 + \frac{100.0}{SNR_i}\right)}. \quad (3)$$

The model covariance matrix, C_M , was constructed from a slowness covariance value, σ , representing the allowable variance of slowness values, and a spatial smoothing value, L , as follows

$$C_{M,ij} = \sigma \cdot \exp\left(\frac{-x_{ij}}{2L^2}\right), \quad (4)$$

where x_{ij} is the squared distance between grid blocks i and j . A diagonal norm damping matrix was constructed by multiplying the norm damping value, ϵ , by the identity matrix, I , and was added to the inverse covariance matrix, C_M^{-1} , to suppress large amplitude slowness values and stabilize the inversion. The ϵ , L , and σ values were all free parameters, found by minimizing the trade-off between data misfit and model size.

Our study area was divided into 10-by-10-km grid cells, or pixels. To maintain inversion stability, we produced the final 2-D group velocity maps in two steps. In the first step, we constructed an initial slowness model from the average slowness across the network. We then inverted using very large smoothing and

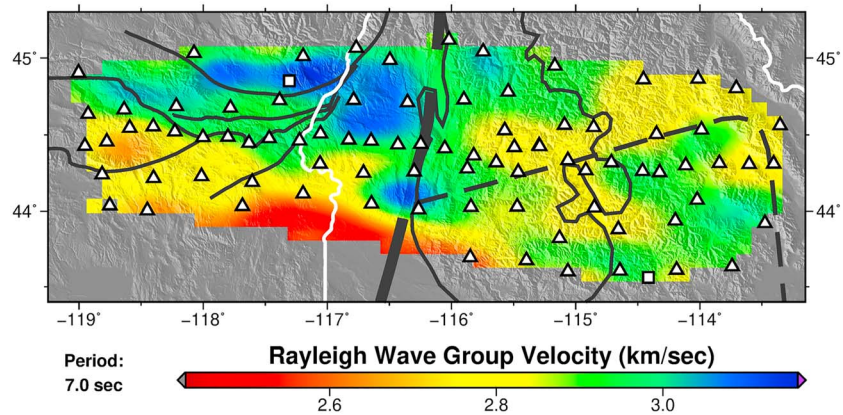


Figure 5. The 2-D group velocity map for 7.0-s period velocity measurements. The map was produced using the two-step inversion procedure outlined in the text. The white lines indicate state borders, and the dark gray lines indicate the major terrane/province boundaries plus the western Idaho shear zone, as shown in Figure 1.

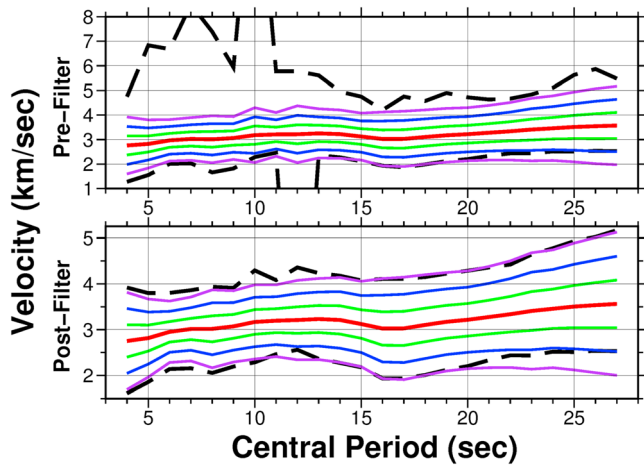


Figure 6. Vertical component network-averaged phase velocity dispersion curves. The bottom panel shows velocity dispersion after filtering data from the top panel to $\pm 3\sigma$. The red lines show mean velocity; green, blue, and purple lines show the ± 1 , 2, and 3σ deviations, respectively; and the black dashed lines show the min/max velocities.

Bessel function under the far-field approximation (Lin et al., 2008). The $N \cdot 2\pi$ term represents the number, N , of full 2π phase cycles for a given phase measurement (or cycle skipping) and must be determined (see below). Finally, the phase traveltimes were calculated as r/c .

We used a damped least squares approach to solve for N as a function of period. We incorporated smoothing to avoid extreme fluctuations of N for neighboring periods. The N curve for each station pair was determined based on the best fit between the resulting phase velocity dispersion curve and the reference dispersion curve (discussed below). There were two iterations of determining N , starting first with an initial reference dispersion curve, then repeating with a set of revised dispersion curves unique to each station pair path.

The first iteration solved for $N(\text{period})$ for each station pair using an initial reference network-averaged phase velocity dispersion curve. To obtain the reference curve, we started with a 1-D network-averaged V_s velocity model derived using receiver functions from the IDOR data set (Stanciu, 2015). We used the V_s model as a starting model to invert for a new V_s from the final network-averaged group velocity dispersion curve (Herrmann, 2013). We then estimated the initial reference network-averaged phase velocity dispersion curve from our new 1-D V_s model. We solved for $N(\text{period})$ for each station pair using this initial reference

overdamping. In the second step, we used the output of the previous step as the new 2-D starting model and inverted using 30-km smoothing and reduced damping. Figure 5 shows one such 2-D group velocity map from inverting the 7.0-s measurements through this two-step process.

3.3. Phase Velocity Measurements and 2-D Maps

Phase velocities were calculated based on the single-station method outlined in Lin et al. (2008), using the analytical complex waveform, where the real portion is the EGF and the imaginary portion is its Hilbert transform, $f_H(t)$. These were used to construct the complex function $A(t)\exp[i\phi(t)]$, where $A(t)$ is an amplitude function and $\phi(t)$ is the phase function. The phase velocity, c , was then calculated at the group travel-time, t_{\max} , as

$$c = \frac{\omega}{k} = \frac{r\omega}{\left[\phi(t_{\max}) + \omega t_{\max} - \frac{\pi}{4} - N \cdot 2\pi - \lambda\right]}, \quad (5)$$

where ω is the instantaneous frequency at t_{\max} , r is the interstation distance, $\phi(t_{\max})$ is the phase function evaluated at t_{\max} , and the source phase ambiguity term (initial phase), λ , is set to 0, as in Lin et al. (2008). The $-\frac{\pi}{4}$ term accounts for both the $\frac{\pi}{2}$ net phase shift between the displacement and the force, and the $-\frac{\pi}{4}$ phase shift from the asymptotic remnant of the

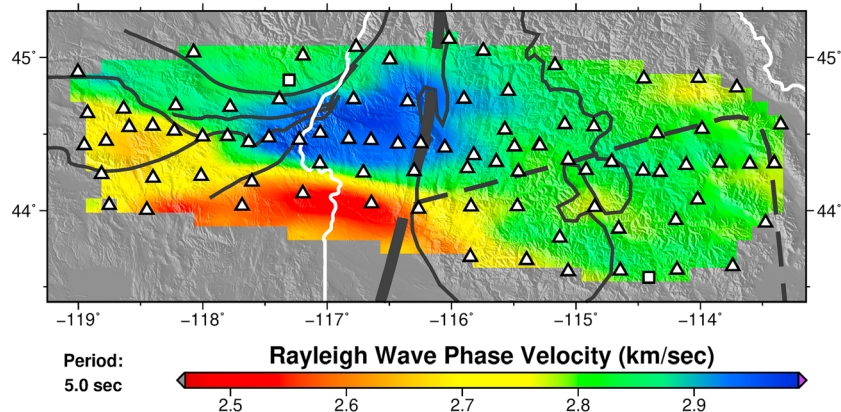


Figure 7. The 2-D phase velocity map for the final set of 5.0-s period velocity measurements (see text for details). The map was produced using the same two-step inversion procedure used for the 2-D group velocity maps. The white lines indicate state borders, and the dark gray lines indicate the major terrane/province boundaries plus the western Idaho shear zone, as shown in Figure 1.

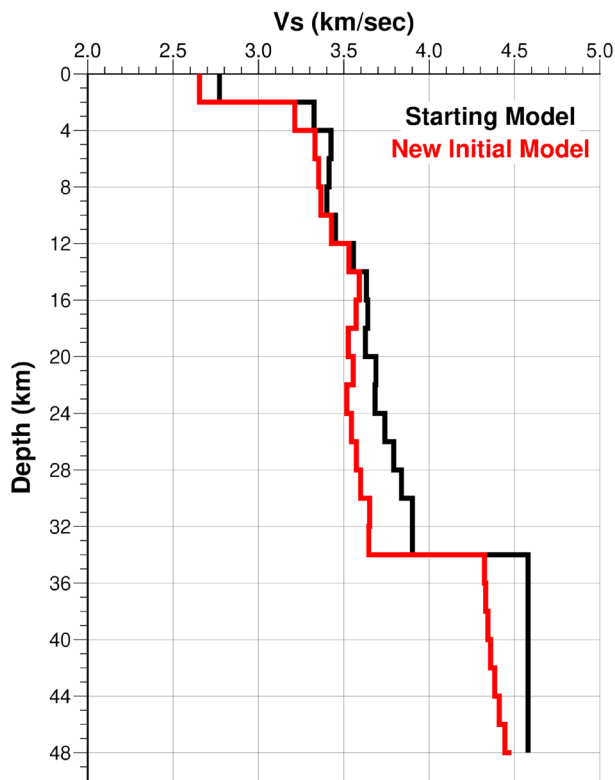


Figure 8. Vertical component 1-D initial model from a joint inversion of both group and phase velocity network-averaged dispersion curves. The starting model used was derived from the best fit V_s model from receiver functions from the IDOR Passive data set (Stanciu, 2015).

mantle velocity beneath the crust to the average P_n velocity found by Buehler & Shearer (2010, 2012) for the IDOR network area. Figure 8 shows the new initial 1-D profile compared to the starting model.

We produced the final 1-D velocity model for each grid pixel from a joint inversion of each pixel's group and phase velocity dispersion curves (Herrmann, 2013). We used the 1-D initial V_s model derived above, but at each pixel updated Moho depth from receiver functions from the IDOR data set (Stanciu et al., 2016), and updated mantle velocity from P_n tomography results (Buehler & Shearer, 2010, 2012). Figure 9 shows the Moho depths and P_n velocities across the IDOR network area used for these updates. Figure 10 shows four examples of our dispersion curve fits to the dispersion measurements and their corresponding final 1-D velocity models after the joint inversion (and after updating Moho depth and P_n velocity). Many of the phase velocity dispersions (from each pixel) featured stronger oscillations or jumps in velocity than their associated group velocity dispersions, likely from difficulties picking the correct value of the cycle skipping term at a given period (see section 3.3). Thus, we elected for a smoother, less stringent fit of the phase velocity dispersions compared to those from the group velocity, which is visible in all four examples shown in Figure 9. For this reason, greater weight was given to the group velocity dispersion curves in the 1-D joint inversions. In the final step, the 1-D profiles were collected to produce the 3-D tomographic model.

4. Results

In the following, we detail the observed S velocity structure in our 3-D tomographic model (Figures 11–13). We provide a full description of the resolution of our model in sections 5.1 and 5.2. However, we note here that structural heterogeneity apparently decreases in the lower crust of the study region, and resolution decreases modestly as well below midcrustal depths. Therefore, for clarity, we truncate cross sections, shown below, at midcrustal depths. However, resolution is sufficiently good to show horizontal velocity variations at deeper crustal levels.

curve, and calculated phase velocities and traveltimes. We calculated 2-D phase velocity maps from all phase velocities and traveltimes within $\pm 3\sigma$ of the network mean using the same method described for the 2-D group velocity maps. In order to reduce possible bias toward the average velocity, new reference dispersion curves were then defined from the path-averaged phase velocity dispersion curves for each station pair from the 2-D phase velocity maps and were used in the second iteration.

The second iteration resulted in only minor adjustments to $N(\text{period})$, consistent with the findings of Lin et al. (2008). New phase velocities and traveltimes were calculated. Figure 6 shows our new network-averaged phase velocity dispersion curves before and after filtering out $\pm 3\sigma$ measurements. As was the case for the 2-D group velocity maps, we produced the final 2-D phase velocity maps in two steps in order to maintain inversion stability, and Figure 7 shows the map resulting from inverting the 5.0-s measurements.

3.4. Three-Dimensional Tomography

We constructed a 3-D tomographic velocity model of the study area from a collection of 1-D velocity profiles from each grid pixel. At each pixel, the inversion proceeded from an initial reference V_s model. The initial V_s model was derived from a joint inversion of both the network-averaged group and phase velocity dispersion curves (Herrmann, 2013) from a starting 1-D velocity model (Figure 8). We used a joint inversion of phase and group velocities because of their different depth sensitivities at a given period, which thus provides better constraints on structure than inverting either alone (Lin et al., 2008; Shapiro & Ritzwoller, 2002). The crustal velocities in the starting model were a network-averaged V_s velocity model derived using receiver functions from the IDOR Passive data set; we also set the Moho depth to 34 km, the average crustal thickness derived from the receiver functions (Stanciu et al., 2016). We set the man-

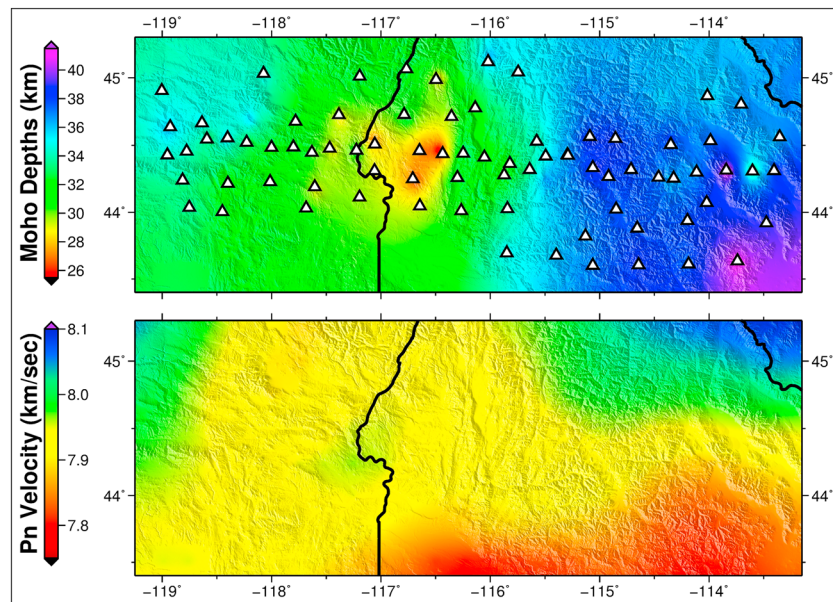


Figure 9. Moho depths and P_n velocities used to update the 1-D initial V_s model. Top panel shows Moho depths across the IDOR network derived from receiver functions on the IDOR Passive data set (Stanciu et al., 2016). Bottom panel shows P_n velocity over the same area (Buehler & Shearer, 2010, 2012).

4.1. Western Idaho Shear Zone (WISZ)

The first-order structure apparent in our ANT crustal model is the obvious difference in upper crustal velocities and architecture between the eastern and western study areas. This difference correlates spatially with the surface outcroppings of the WISZ and persists to at least 15-km depth. We detail these differences, at increasing depths, in the following.

4.1.1. Four-Kilometer Depth

The area beneath the surface expression of the WISZ (surface WISZ) entails a strong velocity contrast in the near surface of the model, with fast S velocities (~ 3.3 km/s) to the west and slower velocities (3.1–3.2 km/s) to the east (Figure 11, top, and Figure 12, A-A', B-B', and C-C'). Correspondence between the strong seismic velocity contrast and the surface WISZ extends from the northern edge to the center of the IDOR footprint. In the southern portion of the model, this pattern is interrupted by a strong slow velocity anomaly coincident with the Western Snake River Plain (Figure 11, top; Figure 12, D-D' for Western Snake River Plain; and Figure 13, H-H').

4.1.2. Twelve-Kilometer Depth

At 12-km depth, the velocity contrast beneath the surface WISZ persists and is perhaps even more pronounced: V_s is ~ 3.6 km/s to the west and ~ 3.45 km/s east of the surface WISZ. In the southern portion of the crustal model, the slow anomaly apparent at 4-km depth beneath the Western Snake River Plain area is no longer present; this area instead also exhibits a clear east-west velocity contrast, with higher velocities to the west of the surface WISZ. (Figure 11, middle; Figure 12, D-D' for Western Snake River Plain; and Figure 13, H-H').

4.1.3. Twenty-Kilometer Depth

By 20-km depth, the contrast in velocity across the surface WISZ is muted and has even changed polarity. The northern to midlatitude region of the IDOR footprint is seismically slow relative to structure east of the surface WISZ. The southernmost portions of the model apparently retain a fast anomaly that stretches well west and east of the surface WISZ (Figure 11, bottom). We note, however, that this apparent anomaly is outside of the perimeter of the network.

4.2. Precambrian North America

East of the surface WISZ, the region of IB outcrops appears as a coherent average-to-slightly-fast velocity body. V_s at 4-km depth within the IB footprint is ~ 3.1 – 3.2 km/s and increases to 3.4–3.5 km/s at 12-km depth and then to ~ 3.6 km/s at 20 km (Figures 11 and 12). At 4-km depth, the perimeter of the IB appears to be slightly faster than its central region; spatially this fast anomaly corresponds to outcrops of the early

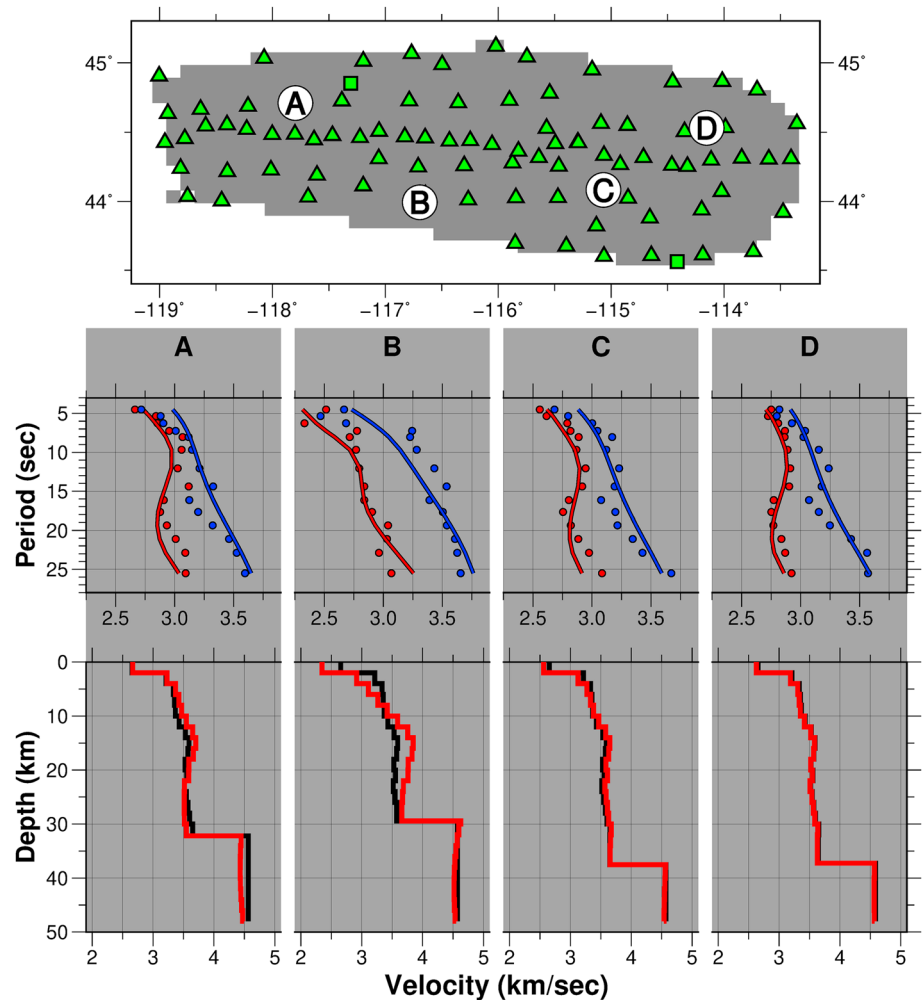


Figure 10. Four dispersion curves relative to the dispersion measurements and their corresponding 1-D velocity models from a joint inversion of group and phase velocity. (top) Geographic location of the four curves (A, B, C, and D) shown in the middle and bottom panels. (middle) Solid lines are calculated dispersion curves for both group (red) and phase (blue) dispersion measurements (circles). (bottom) Corresponding initial (black) and final (red) 1-D velocity models, both of which include updated Moho depth and P_n velocity. Generally, we allowed a smoother fit to the phase velocity dispersions than we did for their associated group velocity dispersions. Greater weight was given to the group velocity dispersion curves in the 1-D joint inversions.

metaluminous and border zone suites of the IB (Figure 11). Seismic velocities similar to those of the IB underlie most of the outcrop area of the Challis volcanic center, at 4-km depth (Figures 11, 12, and 13, I-I').

4.3. Blue Mountains Terranes

4.3.1. Wallowa Arc Terrane

The Wallowa terrane subsurface is seismically fast, $V_s \sim 3.3$ increasing to 3.6 km/s, from near surface to below 12-km depth (Figures 11–13). At 4-km depth, seismic velocities of the Wallowa terrane subsurface are difficult to distinguish from those of the Olds Ferry and Bourne subterrane. The velocity contrast between the Wallowa subsurface units and those of the Bourne and Olds Ferry is stronger at 12 km. By 20-km depth, the crust beneath the Wallowa terrane outcrop area attains the average network velocity.

4.3.2. Baker Terrane

At 4-km depth, the Baker terrane subsurface can be divided into a fast velocity ($V_s \sim 3.2$ –3.3 km/s) body spatially correlated with the Bourne and Burnt River Schist subterrane and a strong slow velocity ($V_s \sim 2.9$ –3.0 km/s) anomaly spatially associated with the Greenhorn subterrane. This distinction largely disappears at 12-km depth, where nearly the entire Baker terrane area subsurface is seismically fast, $V_s \sim 3.5$ –3.6 km/s, although the southern portion of the Greenhorn subterrane area is average velocity, $V_s \approx 3.45$ km/s. At 20-km depth, most of the Baker terrane area subsurface is characterized by

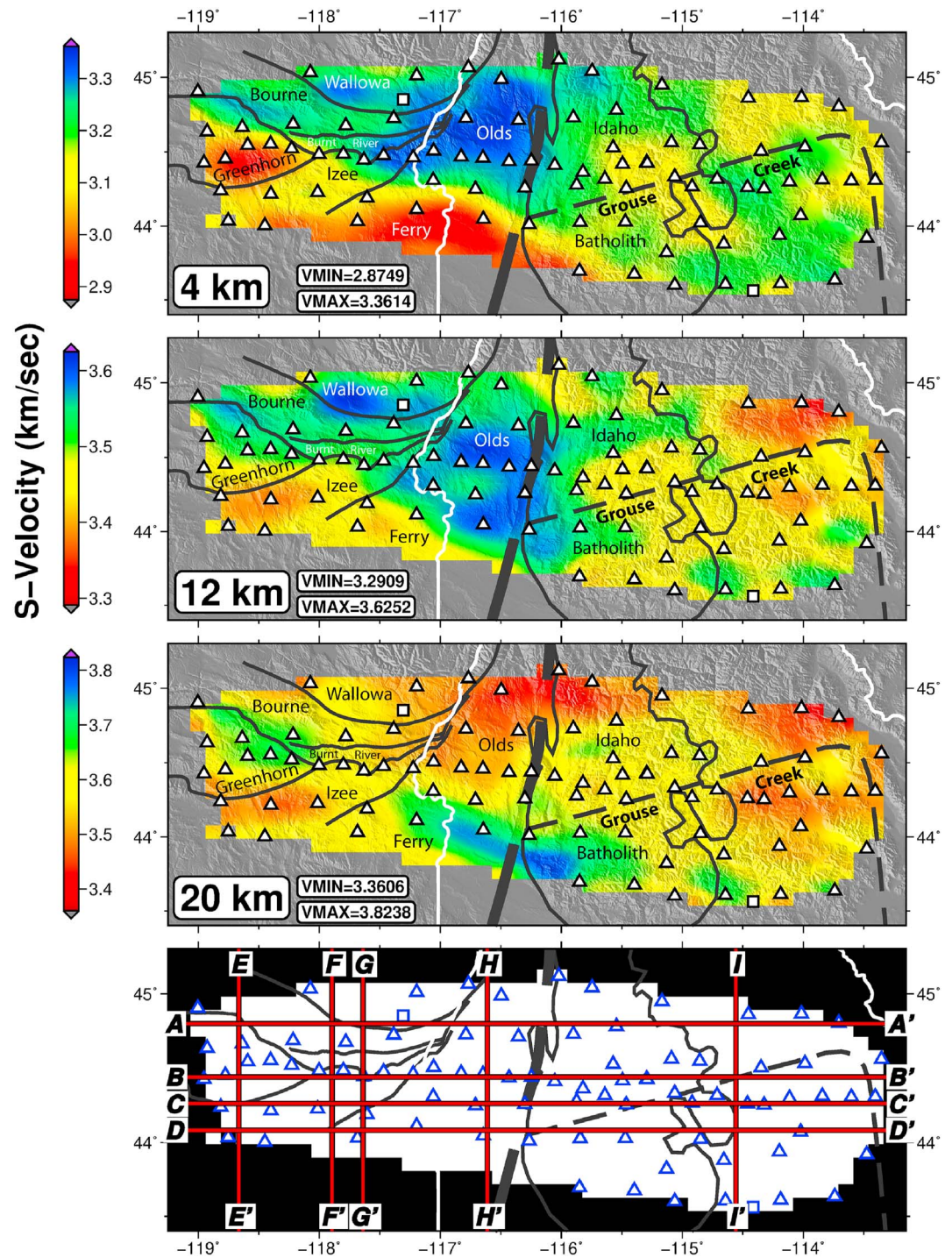


Figure 11. Vertical component depth slices (4, 12, and 20 km) of the 3-D tomography (top three panels) with labeled terrane/province boundaries from Figure 1 for context. (bottom) Cross-section lines shown in Figures 12 and 13.

$V_s \sim 3.55\text{--}3.60$ km/s, although the area beneath the Bourne-Greenhorn border is seismically faster, $V_s = 3.65$ km/s (Figures 11, 12 A-A' and B-B', and 13 E-E', F-F', and G-G').

4.3.3. Izee

Except for a portion of its northeasternmost outcrop area, the subsurface of the Izee terrane is characterized by relatively low seismic velocities, $V_s \sim 3.1$ km/s at 4-km depth, 3.4 km/s at 12-km depth, and 3.5 km/s at 20-km depth. The apparent fast seismic velocities in the northeastern Izee terrane subsurface may be

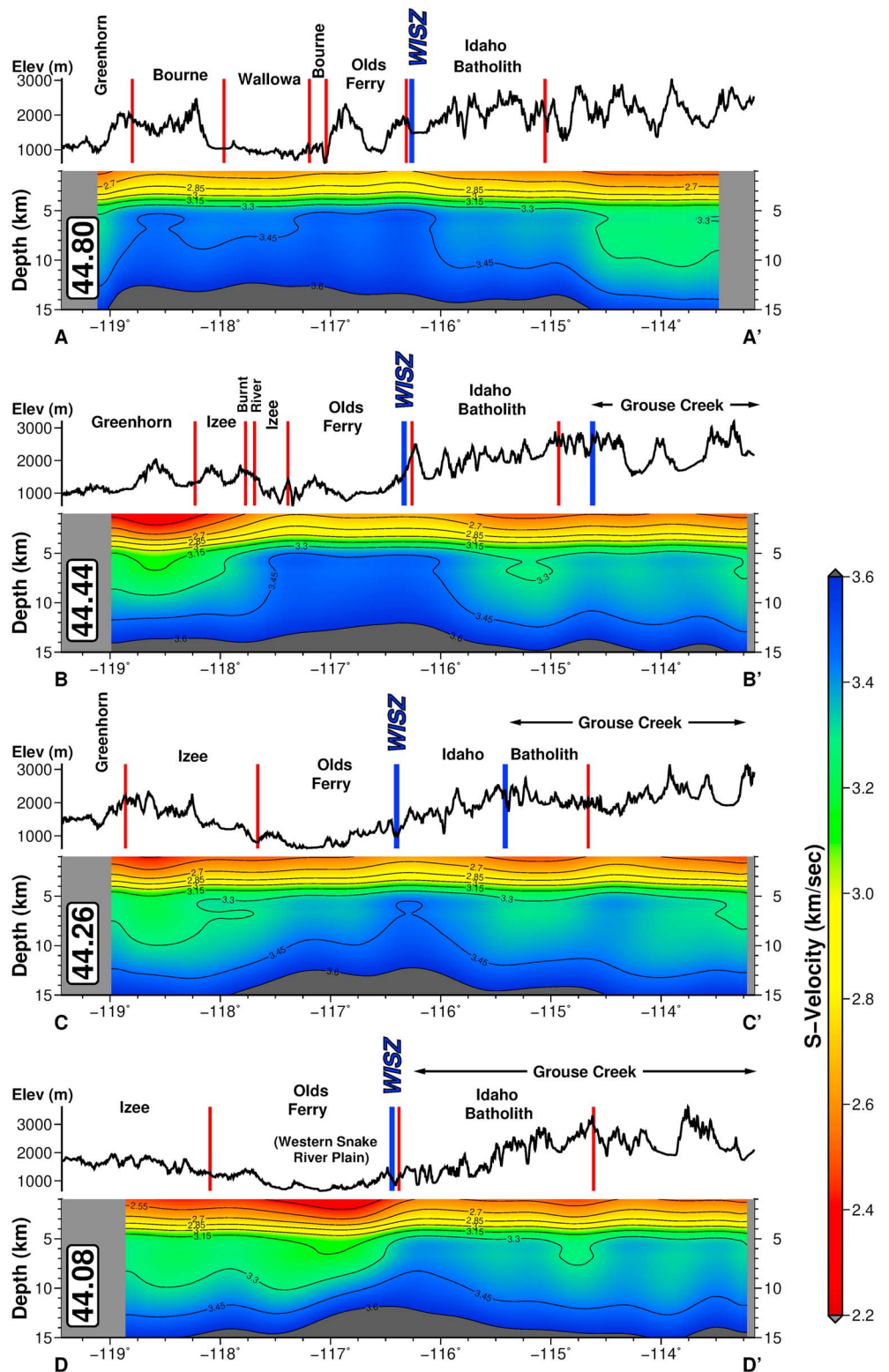


Figure 12. East-west cross sections of 3-D ambient noise tomography. Boxed numbers indicate latitude of each cross section; section lines shown in bottom panel of Figure 11. Top of each panel shows elevation across profile with surficial geologic boundaries marked. WISZ = western Idaho shear zone.

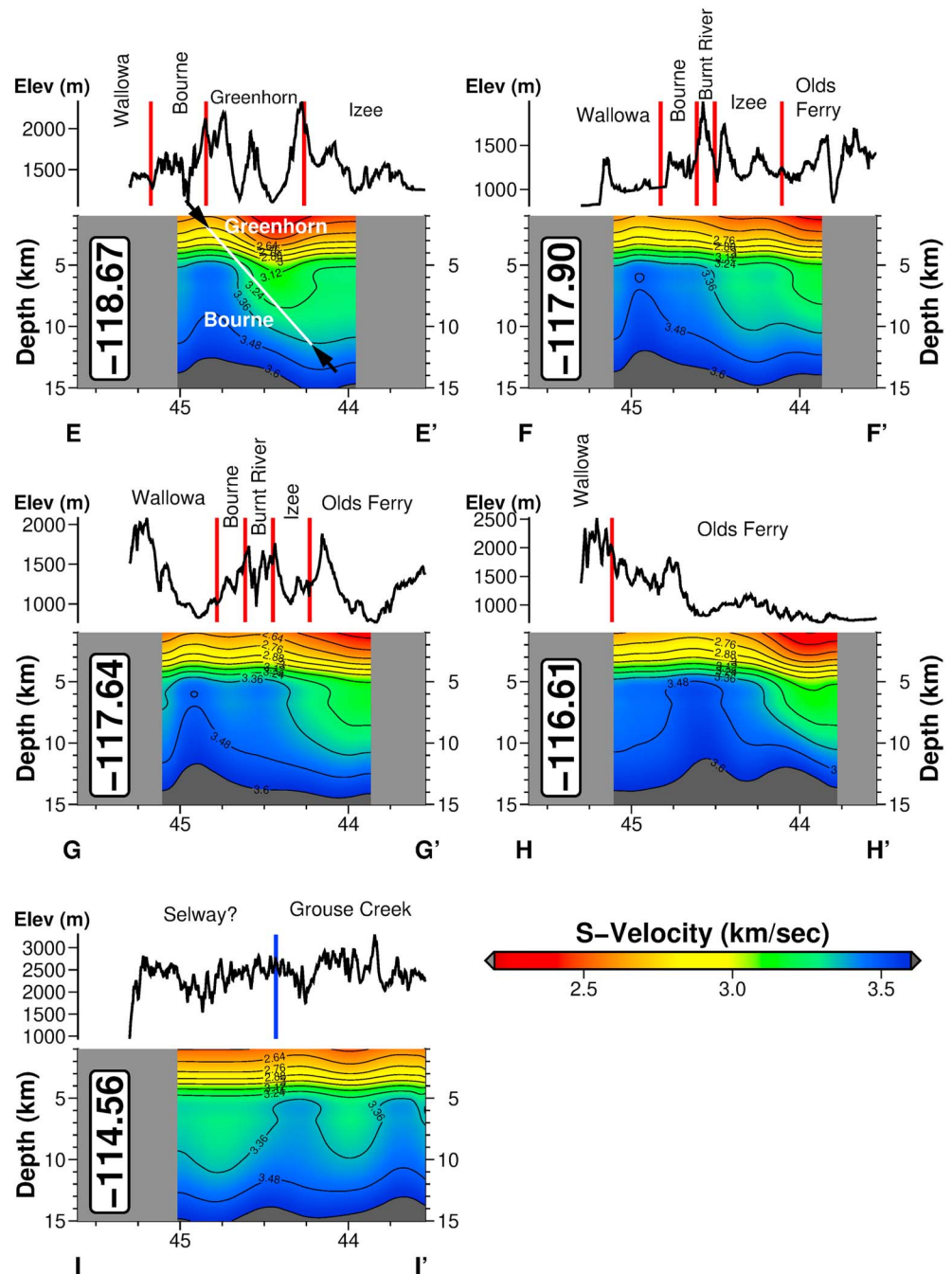


Figure 13. North-south cross sections of 3-D ambient noise tomography. Boxed numbers indicate longitude of each cross section; section lines shown in bottom panel of Figure 11. Top of each panel shows elevation across profile with surficial geologic boundaries marked.

artifacts of low resolution (see below), as the total outcrop area is comparable to the station spacing in this area (Figures 11 and 13, F-F' and G-G').

4.3.4. Olds Ferry Arc Terrane

The subsurface of the Olds Ferry terrane is characterized by fast seismic velocities at 4-km depth, except where the terrane is covered by deposits within the Western Snake River Plain graben. At 12-km depth, nearly the entire Olds Ferry subsurface is relatively seismically fast, $V_s \sim 3.5\text{--}3.6$ km/s. At 20-km depth, the velocity of the Olds Ferry terrane subsurface is apparently relatively slow, $V_s = 3.55$ km/s, on average (Figures 11 and 12).

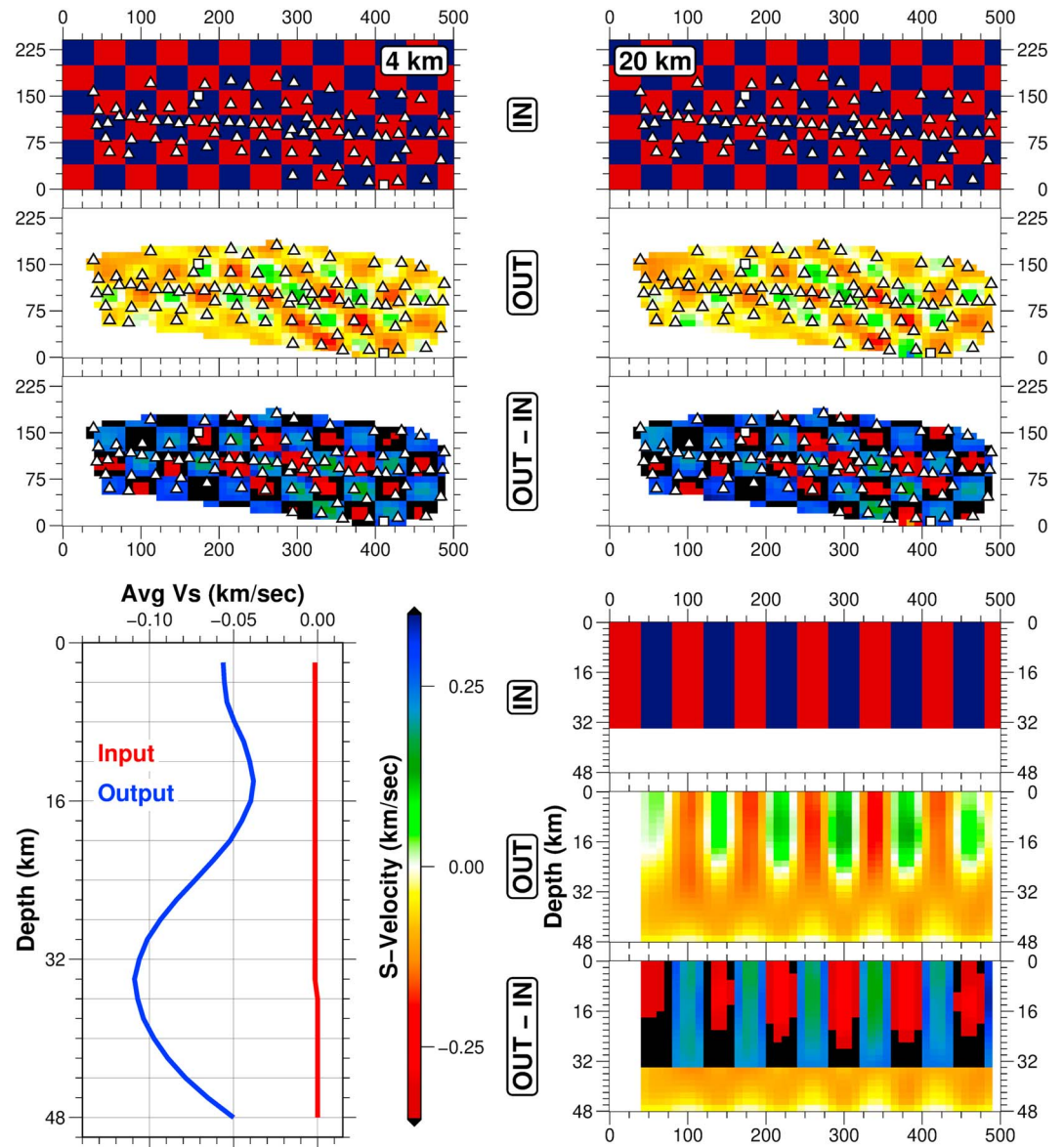


Figure 14. Results of checkerboard resolution test with a two-layer input model: Layers 1 and 2 are 34 and 14 km thick, respectively. V_s in the upper layer alternates $\pm 35\%$ about the network mean velocity within blocks 40×40 km on a side. The lower layer is network mean velocity. Top two panels: 4- and 20-km depth slices. Bottom two panels: west-east cross sections (right) along the 105.0-km E-W line (see top panel maps) and associated network-averaged depth profile (left) used in section 5.2 (see text for details). IN = input model; OUT = output model; OUT-IN = output-input model difference.

5. Discussion

5.1. Resolution Tests

We performed multiple checkerboard resolution tests to determine if we are precluded from imaging existing crustal structure either by our method or our data set. We show results of four such tests: In each test, blocks in the model crustal layers are 34 km thick and 40×40 km on a side. Seismic velocities within alternating blocks are perturbed $\pm 35\%$ from the final network-average 1-D velocity model, and the blocks are underlain by a 14-km mantle layer with zero perturbation (no added structure). For each test scenario, we forward calculated synthetic data, d_{syn} , by multiplying the kernel matrix, G , saved from the 2-D group and phase velocity inversions with the checkerboard test model, M_{cb} , and then adding noise, d_{noise} , as

$$d_{\text{syn}} = GM_{\text{cb}} + d_{\text{noise}}. \quad (6)$$

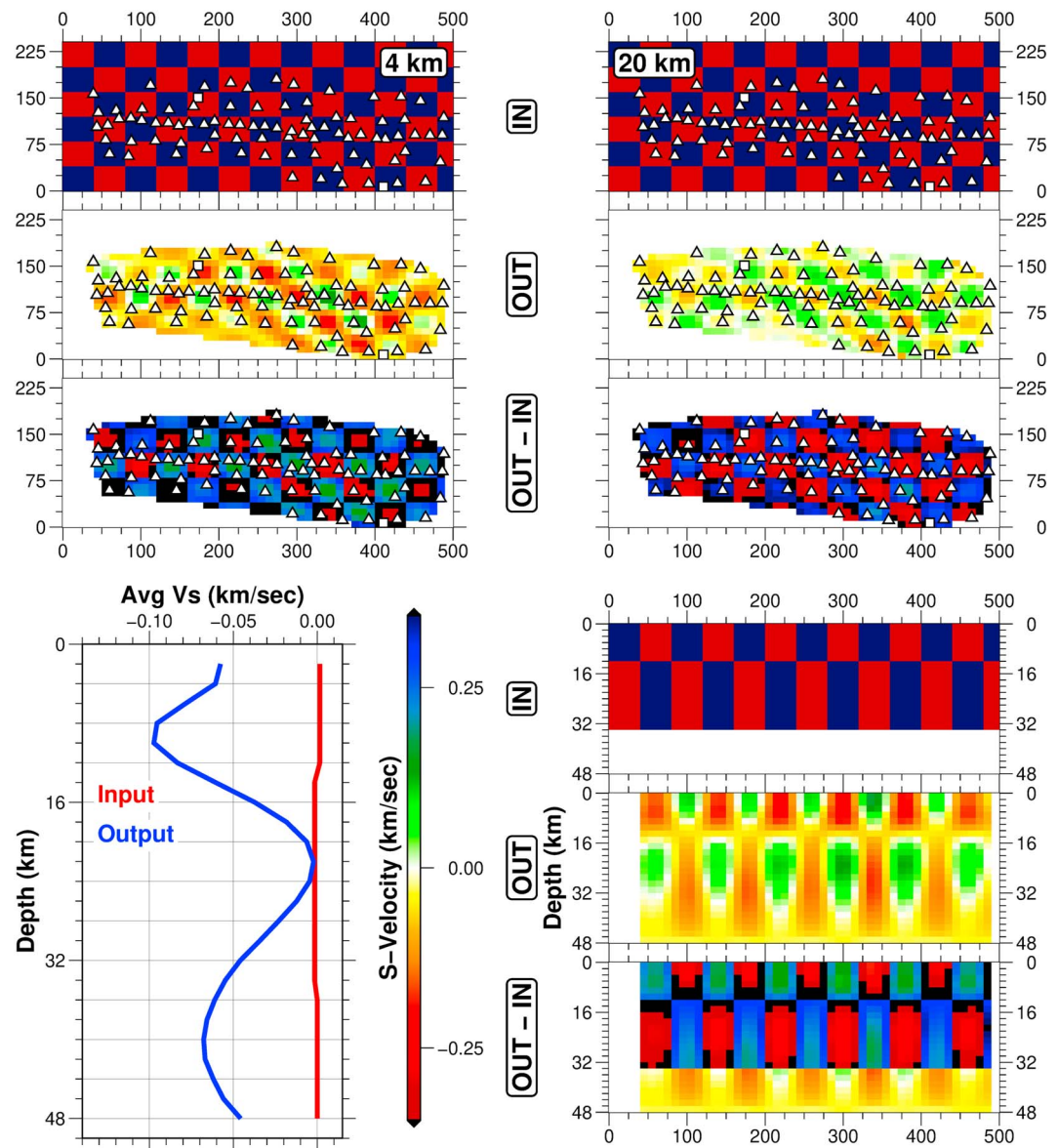


Figure 15. Same as Figure 14 but for a three-layer input model: Layer 1 is 12 km thick, layer 2 is 22 km thick, and layer 3 is 14 km thick. IN = input model; OUT = output model; OUT-IN = output-input model difference.

We repeated this for each period, and inverted for the corresponding 2-D group and phase velocity maps as outlined in section 3.2.2, and using the same inversion parameters as those used for the observed data. The 3-D tomographic models were then produced in the same way as detailed in section 3.4. Figures 14–17 show cross sections and depth slices for each of these resolution test results, as well as a corresponding network-averaged 1-D velocity profile that is used in section 5.2.

The resolution tests in Figure 14 show that the method and data set are capable of resolving strong sub-vertical velocity contrasts that extend through the whole crust. To a degree, the inversions extend structure spuriously into the mantle. Figure 15 shows that a vertical structure that is interrupted, or offset, at 12-km depth (Figures 11 and 12) but that then continues to the base of the crust, is well resolved. Figure 16 shows that structures present solely in the lower crust are not well resolved. These tests show that vertical resolution drops off significantly below midcrustal depths; however, they also clearly demonstrate that a strong vertical velocity contrast through the entire crust beneath the surface WISZ would be resolvable, if present, calling into question the notion of a WISZ characterized by a strong cross-structure velocity contrast extending through the entire crust.

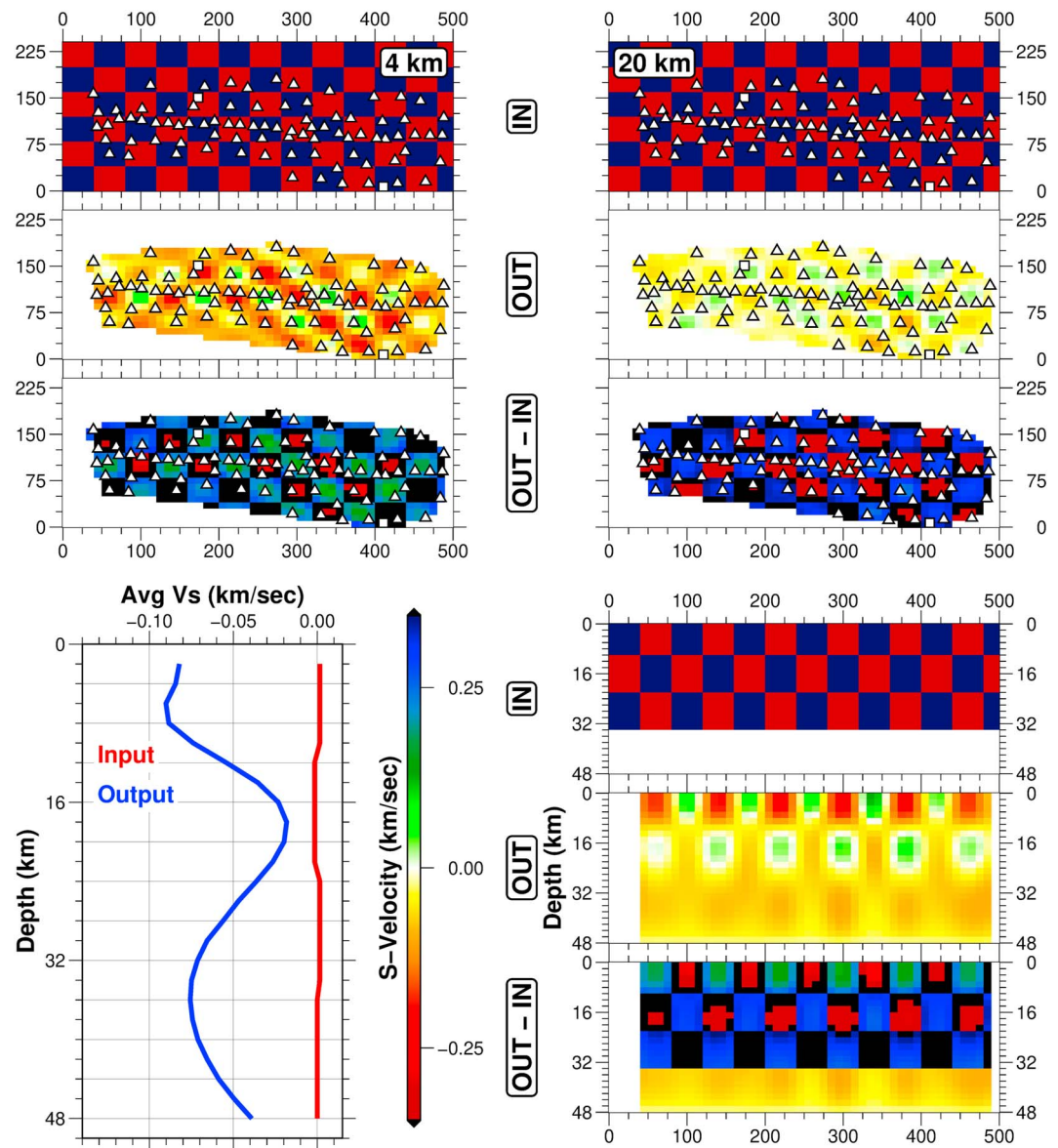


Figure 16. Same as Figure 14 but for an input model of four layers, 10, 12, 12, and 14 km thick, respectively. IN = input model; OUT = output model; OUT-IN = output-input model difference.

5.2. Damping Bias, Shear Velocities, V_p/V_s , and Poisson's Ratio

We estimated the depth-dependent bias toward slower velocities induced by our inversion methods, using the differences between network-averaged results of recovered checkerboard blocks and those of the input model. Because we solved the linear 2-D inversion for slowness, rather than velocity, damping of the inversion-biased results toward lower velocities. The applied damping has a greater impact on higher velocities, an effect visible in all our resolution tests (lower left panel in each of Figures 14–17). Relative to the unperturbed network-averaged velocities, the recovered velocities can be as much as 0.1 km/s slow. Depending on the details of the perturbed input structure model, the minimum difference between input and recovered structure localizes at midcrustal depths, 10–20 km below surface. Recovered shallow crustal velocities, 0–10 km deep, are systematically reduced relative to the input model, as are those deeper than ~18 km, and in order to compare these results to shear velocities of common lithologies or to results from other seismic studies (e.g., Davenport et al., 2017), they should be adjusted upward by 0.05–0.1 km/s (Table 1). The combination of our inversion shear velocities and compressional wave velocities obtained by Davenport et al. (2017) allows calculation of V_p/V_s and Poisson's ratio, ν , for the various tectonic units sampled by the two seismic experiments. We emphasize that the strictly linear nature of the IDOR-controlled

source seismic experiment (Davenport et al., 2017), whose results derive from only a narrowband of latitudes on either side of the largely E-W line of deployed geophones, restricts the area for which these calculations are valid. However, the major tectonic units of the study area, the Wallowa arc terrane excepted, were adequately sampled by both the IDOR active and passive source experiments. Given both V_p and V_s ,

$$\nu = \frac{V_p^2 - 2V_s^2}{2(V_p^2 - V_s^2)}. \quad (7)$$

We provide two estimates of ν in Table 1, one calculated using the V_s determined in the 3-D inversion (Calc. 1 column) and a second using this V_s adjusted to higher velocity to rectify the bias toward slower velocities caused by the applied damping (Calc. 2 column). Shear velocities at 4- and 20-km depths determined from the 3-D inversion were increased by 0.1 km/s; those for 12-km depths were increased 0.05 km/s. V_p/V_s calculated from values we estimate and those of Davenport et al. (2017), and from the receiver function study of Stanciu et al. (2016), are also reported in Table 1.

The Poisson's ratios, ν , in Table 1 are similar to those reported in seismic studies—both laboratory and field based—of continental lithologies (Christensen, 1996; Holbrook et al., 1999; Kern, 2011; Lombardi et al., 2008; Miller & Christensen, 1994). However, the shallow to midcrustal depth V_p/V_s ratios we calculate are consistently higher than the V_p/V_s (κ values, from the h- κ method of Zhu & Kanamori, 2000) determined by Stanciu et al. (2016) for the IDOR area. Note that the latter V_p/V_s values are representative of the entire crustal column sampled by the mode-converted and reverberating phases used in the h- κ receiver function method, whereas the V_p/V_s ratios we present are representative of the upper to midcrust, due to resolution loss at lower crustal depths. Higher V_p/V_s ratios from the ANT results, relative to those derived from the receiver functions, are likely due to the presence of low velocity sediments, and pervasively fractured and low-grade metamorphosed near-surface rocks that are well sampled by the diffusive wavefield but contribute relatively little to receiver function h- κ estimations that reflect the entire crustal column.

In general, the shear velocities, Poisson's ratios, and V_p/V_s ratios we calculate are consistent with the inferred lithologies of the tectonic units in the IDOR study area: For example, the IB is characterized by shear velocities ranging from 3.4–3.7 km/s from shallow to midcrustal depths, as determined by our ANT inversion; V_p/V_s ranges from 1.68–1.71; and ν varies from 0.223–0.242. In comparison, values for granitic lithologies at upper crustal pressures are \sim 3.7 km/s, 1.702–1.710, and 0.237–0.240, as determined by Christensen (1996).

Although Davenport et al. (2017) show that P -wave velocities in the IB are constant through the midcrust, the ANT results indicate that V_s increases in the midcrust (Figure 12), perhaps indicative of increasing seismic anisotropy in the deeper batholith, which tends to be more deformed, or below it within Precambrian gneisses (e.g., Stanciu et al., 2016), which affects V_s more than V_p .

5.3. Western Idaho Shear Zone

The crustal velocity model we derive reveals a clear velocity contrast across the surface trace of the WISZ. We interpret this result as a continuous near-vertical WISZ, forming a crustal break from shallow to at least midcrustal depths (Figures 11 and 12). Results from IDOR Passive source receiver functions (Stanciu et al., 2016) and IDOR active source refraction tomography (Davenport et al., 2017) did resolve a Moho offset beneath the surface WISZ, indicating that near-vertical crustal truncation likely does extend through the entire crust. This result is consistent with a sharp boundary in the radiogenic isotopic ratios of Cretaceous to Miocene igneous rocks east and west of the WISZ. However, our ANT results do not positively indicate a sub-vertical structural boundary through the entire crust. Instead, the velocity contrast between Blue Mountains terranes juxtaposed against continental North America at the WISZ becomes indistinct deeper than around 15 km. This result is not unexpected, though, since Davenport et al. (2017) detected a <0.2 -km/s velocity contrast across the WISZ at depths from \sim 20 km to the Moho, using high-resolution controlled-source P -wave traveltimes measurements. Given the reduced resolution at mid-lower crustal depths of our noise tomography, a velocity contrast of this magnitude is likely to be unresolved. Thus, we prefer the interpretation that the WISZ represents a structural boundary between the Olds Ferry island arc and continental North America and that a strong velocity contrast across the WISZ extends through the shallow-to-middle crust with a minor velocity contrast in the lower crust.

5.4. Arc Terranes, Continental North America, and Continental Growth

We note that the WISZ juxtaposes tectonostratigraphic units of intraoceanic arc (Wallowa terrane) and pericratonic arc (Baker and Olds Ferry terrane) against the IB, composed of S-type granitoids, predominantly

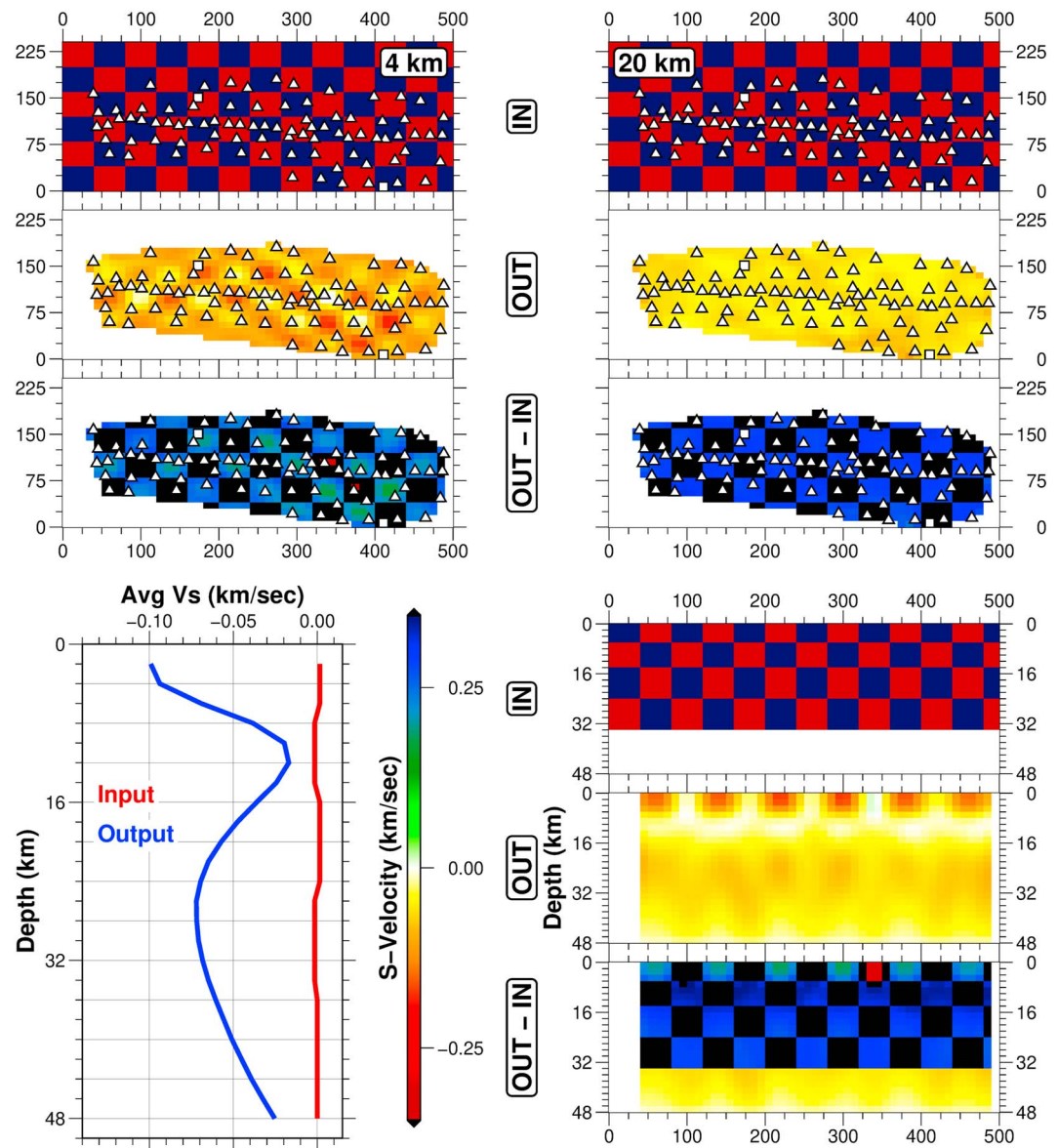


Figure 17. Same as Figure 14 but for an input model of five layers, 6, 8, 10, 10, and 14 km thick, respectively. IN = input model; OUT = output model; OUT-IN = output-input model difference.

continental shelf sediments and crust largely melted in place on the early Paleozoic passive margin (Gaschnig et al., 2011; Lund, 2008). The Archean Grouse Creek block is basement to the batholith itself (Foster et al., 2006; Gaschnig et al., 2013), and thus, at lower crustal depths abuts the Olds Ferry terrane at the WISZ, where both our results and those of Davenport et al. (2017) show little velocity contrast between the Olds Ferry arc and the Grouse Creek block. V_p in the deep Olds Ferry terrane is ~ 6.4 km/s (Davenport et al., 2017), and V_s is ~ 3.65 km/s (Table 1). Although there is not a V_p estimate for the Wallowa arc terrane (not sampled by Davenport et al., 2017), V_s from our ANT results for the Wallowa intraoceanic arc is also ~ 3.65 km/s (Table 1). For the IB/Grouse Creek deep crust, V_p is ~ 6.2 km/s, and V_s is ~ 3.7 km/s. Thus, down to midcrust, the observed seismic velocities for all three units—the intraoceanic Wallowa arc, the pericratonic Olds Ferry arc, and the IB continental arc—are consistent with a predominantly felsic petrology (e.g., Miller & Christensen, 1994) on both sides of the deep WISZ and in the Wallowa terrane.

Comparison of our results from the two Blue Mountains arc terranes with currently active arcs and other arc terranes is instructive: Active source studies of the Aleutians arc (Holbrook et al., 1999; Shillington et al., 2004) and the Izu-Bonin-Mariana arc (Takahashi et al., 2007; Suyehiro et al., 1996) indicate that arc

Table 1

Comparison of V_p/V_s Values From Stanciu et al. (2016) Against Calculated Values of Both V_p/V_s and Poisson's Ratios using V_p from Davenport et al. (2017) and V_s From This Study

Tectonic unit	This study		Davenport et al. (2017)	Stanciu et al. (2016)	This study		
	V_s Obs. (km/s)	V_s Adj. (km/s)	V_p Obs. (km/s)	V_p/V_s	V_p/V_s	ν Calc. 1	ν Calc. 2
4-km depth							
Idaho Bath/E WISZ	3.2–3.3	3.4	5.8	1.65	1.71	0.261	0.238
Olds Ferry/W WISZ	3.3	3.4	6.0	1.76	1.76	0.283	0.264
Idaho Bath/Challis	3.1–3.2	3.2–3.3	5.8	1.70	1.76	0.281	0.261
Olds Ferry	3.3	3.4	6.0	1.68	1.76	0.283	0.264
Wallowa	3.3	3.4	—	1.73	—	—	—
Baker:Greenhorn	2.9–3.0	3.0–3.1	6.0	1.74	1.93	0.348	0.333
Izee	3.1	3.2	6.0	1.67	1.88	0.301	0.283
12-km depth							
Idaho Bath/E WISZ	3.45	3.50	6.0	1.65	1.71	0.253	0.242
Olds Ferry/W WISZ	3.6	3.65	6.25	1.76	1.71	0.252	0.241
Idaho Bath/Challis	3.4–3.5	3.45–3.55	6.0	1.70	1.71	0.242	0.231
Olds Ferry	3.5–3.6	3.55–3.65	6.4	1.68	1.78	0.269	0.259
Wallowa	3.6	3.65	—	1.73	—	—	—
Baker:BR	3.5–3.6	3.55–3.65	6.4	1.70	1.78	0.269	0.259
Baker:Greenhorn	3.45	3.50	6.4	1.74	1.83	0.295	0.287
Izee	3.4	3.45	6.4	1.67	1.86	0.303	0.295
20-km depth							
Idaho Bath/Challis	3.6	3.7	6.2	1.65	1.68	0.246	0.223
Olds Ferry	3.55	3.65	6.4	1.76	1.75	0.278	0.259
Wallowa	3.5–3.6	3.6–3.7	—	1.73	—	—	—
Baker:BR	3.55–3.60	3.65–3.75	6.4	1.70	1.73	0.269	0.249
Bourne-Greenhorn	3.65	3.75	6.4	1.74	1.71	0.259	0.239
Izee	3.5	3.6	—	1.67	—	—	—

Note. WISZ = Western Idaho shear zone.

composition is variable and may include predominantly mafic rocks, as in the Aleutians, but also layered structure including shallow volcanics, a relatively thick and felsic (tonalite) plutonic complex, and more mafic lower crustal rocks, as in the Izu-Bonin-Marianas. Thus, these results differ significantly from those of our study and Davenport et al. (2017), which show that felsic rocks dominate apparently the entire crustal column of the Olds Ferry arc and Wallowa arcs. Seismological and field studies show that the Mesozoic Kohistan intraoceanic arc is composed of a felsic (granodiorite and tonalite) upper-midcrustal layer ~10–15 km thick above mafic (meta-)cumulates that were the residuum from which the felsic Kohistan units were derived (Miller & Christensen, 1994). The lowermost crustal mafic units are seismically indistinguishable from the underlying mantle rocks but are petrologically distinct and clearly lie above a deeper, true Moho. Given that crustal thicknesses beneath both the Olds Ferry and Wallowa terranes are 28–36 km (Stanciu et al., 2016) and given low seismic velocities that imply felsic compositions of the two arc terranes to the apparent Moho, we suggest that the Kohistan and Izu-Bonin-Marianas arcs are viable analogs for the Olds Ferry and Wallowa arc terranes. If so, the Olds Ferry and/or Wallowa arcs must have included more mafic lower crustal units, but these units may have been stripped off and subducted during Mesozoic accretion or subsequently delaminated (Kay & Kay, 1993). If so, how are crustal thicknesses of >30 km from the accreted felsic units of the two arcs achieved? We note that in outcrop neither arc terrane approaches the width of current active arcs (~100 km, max, for the Blue Mountains arcs, versus >450 km, for example, for the Izu arc), and thus, one possible mechanism for attaining apparently normal continental crustal thicknesses is to imbricate and thicken the midcrustal plutonic complexes of the Mesozoic arcs during and after accretion. There is some evidence for such shortening in the Olds Ferry terrane, which includes apparently

significant thrust faults unrelated to post-accretion history (Kurz et al., 2017). Given the relatively short life span of the Blue Mountains arcs, we consider it unlikely that 30+ km of felsic plutonic complex accumulated and is preserved intact today.

ANT results from stations sited on the Selway terrane, in the northeastern portions of the IDOR footprint, show that the upper-midcrustal portions of the Selway are characterized by relatively low shear wave velocities, ~ 3.2 km/s at 4-km depth, rising to ~ 3.5 km/s at 20 km. These velocities are even slower than those of the IB and its Grouse Creek block basement. Such low velocities are consistent with a felsic upper to midcrust and indicate that the Precambrian basement, preserved in this region, was apparently largely unmodified by any significant mafic Eocene Challis magmatism or that Eocene felsic and postassic Challis plutons comprise much of the upper crust.

5.5. Baker Terrane Structure

The Baker terrane, a subduction mélangé-forearc complex of the Olds Ferry terrane, is subdivided into three distinct tectonostratigraphic units, the Bourne, Burnt River, and Greenhorn subterrane (Schwartz et al., 2011). Our tomographic results clearly show a distinction between the Greenhorn subterrane and its surroundings. At shallow depths, the Bourne and Burnt River Schist subterrane have relatively fast seismic velocities, similar to those of the Wallowa and Olds Ferry arcs; in contrast, the Greenhorn subterrane is seismically slow (Figures 11 top panel and 12 A-A' and B-B'). North-south cross sections in the western IDOR footprint (Figure 13 E-E') show the base of the Greenhorn slow anomaly dips to the south or southeast, and that the Greenhorn is underlain by relatively fast material beneath depths of around 10 km; this high velocity body is continuous with the faster anomaly beneath the Bourne subterrane and extends even to the Wallowa arc terrane subsurface. This geometry implies that the relatively high velocity Bourne subterrane underlies the Greenhorn. The Bourne subterrane is, in turn, the hanging wall in thrust contact over imbricated blocks of the Wallowa arc terrane (Schwartz et al., 2011). The tomography is thus consistent with thrusting of the Bourne and Greenhorn forearc units over the Wallowa arc terrane on south or southeast dipping faults. The relationship of the Baker terrane units and the Olds Ferry arc terrane is unclear.

At least near the border, the Bourne subterrane is thought to be thrust over imbricated blocks of Wallowa (Schwartz et al., 2011) and lends support to the idea that the Bourne fast velocity is the result of remnant oceanic crust or an extension of Wallowa at shallow depths. This also implies that Greenhorn must have at least 10 km of slow velocity material near the surface. Indeed, line B-B' in Figure 12 and line E-E' of Figure 13 show slow velocity down to approximately 10 km and may indicate a thick package of accretionary complex related material or a thick package of forearc basin material at depth, over a further extension of Wallowa related arc or oceanic crust within the midcrust.

6. Conclusions

The depth extent of the WISZ is not constrained by this study, but a strong velocity contrast associated with the WISZ is visible down to midcrustal depths. At lower crustal depths, the velocity contrast between the Olds Ferry arc terrane and the Precambrian North American basement is too small to be resolved. We resolve a strong, shallow, low S velocity anomaly associated with sediment infill in the western Snake River plain graben. Within the central BMP, the Bourne and Greenhorn subterrane of the Baker terrane have distinctly different seismic velocities at shallow crustal depths. The boundary between these two units is resolved in our tomography and dips south or southeast from the near surface to midcrustal depths. We propose that the Bourne subterrane underthrust the Greenhorn subterrane along this surface during accretion to North America.

Seismic velocities of crustal columns in the Olds Ferry and Wallowa arc terranes are relatively low, consistent with felsic petrology to deep crustal levels. Although the Olds Ferry arc may have developed as a continental arc, the Wallowa was clearly an intraoceanic arc, and thus felsic compositions throughout a normal (30+ km) crustal thickness and an absence of seismic velocities clearly consistent with mafic compositions in the mid-lower crust probably resulted from subduction of the original lower crustal units of the two arcs, during accretion, or from delamination of these denser units. The BMP arc terranes may thus have attained their current thick felsic crustal columns by thrust imbrication and shortening and thickening of the upper crustal plutonic complexes of the two arcs. If so, the accretionary style of these arc terranes bears important implications for the processes of continental growth.

Acknowledgments

We are very grateful to Katee Neesmith, Stephanie James, Kathy Davenport, Jon Delph, Katie Garman, and Madeline Job for their strenuous efforts during the IDOR Passive seismic project field work. We are very grateful to George Slad, Noel Barstow, and Pnina Miller of Incorporated Research Institutions for Seismology (IRIS) PASSCAL for their 24/7 field support far above and beyond the call of duty. Basil Tikoff, Jeff Vervoort, Richard Gaschnig, Annia Fayon, John Hole, Reed Lewis, and Mark Fernes provided crucial instruction through helpful discussions of geology, geochronology, and geochemistry and tectonics of the study area and of seismic techniques. The IDOR Passive seismic project would not have been possible without the help and support of the people of Idaho and eastern Oregon, who cheerfully gave us permission to site and access seismic stations on their properties for 2+ years. We are grateful to Elaine Alexander and her colleagues at the U.S. Forest Service and to David Wolf and Tim Vanek of the Bureau of Land Management for their help in permitting. Reviews by Zack Spica, an anonymous reviewer, and the editor were extremely helpful in improving the manuscript. This work is supported by U.S. National Science Foundation grant EAR-0844187. We created all the maps and figures using the Generic Mapping Tools (Wessel & Smith, 1998; Wessel et al., 2013). Data analysis was performed using SAC (Seismic Analysis Code; Goldstein, 2003; Goldstein & Snoke, 2005). The seismic instruments were provided by IRIS through PASSCAL Instrument Center at New Mexico Tech. The seismic data used in this paper are freely available through the IRIS Data Management Center. The facilities of the IRIS Consortium are supported by the National Science Foundation under Cooperative Agreement EAR-1261681.

References

Armstrong, R., & Ward, P. (1991). Evolving geographic patterns of cenozoic magmatism in the North American Cordillera: The temporal and spatial association of magmatism and metamorphic core complexes. *Journal of Geophysical Research*, 96(B8), 13,201–13,224.

Ashley, R. (1995). Petrology and deformation history of the burnt river schist and associated plutonic rocks in the burnt river canyon area, northeastern Oregon. *Geology of the Blue Mountains region of Oregon, Idaho, and Washington: Petrology and tectonic evolution of pre-Tertiary rocks of the Blue Mountains region: US Geological Survey Professional Paper, 1438*, 457–496.

Bensen, G., Ritzwoller, M., Barmin, M., Levshin, A., Lin, F., Moschetti, M., et al. (2007). Processing seismic ambient noise data to obtain reliable broad-band surface wave dispersion measurements. *Geophysical Journal International*, 169(3), 1239–1260. <https://doi.org/10.1111/j.1365-246x.2007.03374.x>

Bond, G. C., Nickeson, P. A., & Kominz, M. A. (1984). Breakup of a supercontinent between 625 Ma and 555 Ma: New evidence and implications for continental histories. *Earth and Planetary Science Letters*, 70(2), 325–345.

Buehler, J. S., & Shearer, P. M. (2010). Pn tomography of the western United States using USArray. *Journal of Geophysical Research*, 115, B09315. <https://doi.org/10.1029/2009JB006874>

Buehler, J., & Shearer, P. (2012). Localized imaging of the uppermost mantle with USArray Pn data. *Journal of Geophysical Research*, 117, B09305. <https://doi.org/10.1029/2012JB009433>

Christensen, N. I. (1996). Poisson's ratio and crustal seismology. *Journal of Geophysical Research*, 101(B2), 3139–3156. <https://doi.org/10.1029/95JB03446>

Colpron, M., Logan, J. M., & Mortensen, J. K. (2002). U-Pb zircon age constraint for late Neoproterozoic rifting and initiation of the lower Paleozoic passive margin of western Laurentia. *Canadian Journal of Earth Sciences*, 39(2), 133–143.

Coney, P. J., & Harms, T. A. (1984). Cordilleran metamorphic core complexes: Cenozoic extensional relics of Mesozoic compression. *Geology*, 12(9), 550–554.

Davenport, K., Hole, J., Tikoff, B., Russo, R., & Harder, S. (2017). A strong contrast in crustal architecture from accreted terranes to craton, constrained by controlled-source seismic data in Idaho and eastern Oregon. *Lithosphere*, 9(2), 325–340.

Dickinson, W. R. (1979). Mesozoic forearc basin in central Oregon. *Geology*, 7(4), 166–170. [https://doi.org/10.1130/0091-7613\(1979\)7<166:MFBICO>2.0.CO;2](https://doi.org/10.1130/0091-7613(1979)7<166:MFBICO>2.0.CO;2)

Dickinson, W. R. (2004). Evolution of the North American Cordillera. *Annual Review of Earth and Planetary Sciences*, 32, 13–45. <https://doi.org/10.1146/annurev.earth.32.101802.120257>

Dorsey, R. J., & LaMaskin, T. A. (2007). Stratigraphic record of Triassic-Jurassic collisional tectonics in the Blue Mountains Province, northeastern Oregon. *American Journal of Science*, 307(10), 1167–1193. <https://doi.org/10.2475/10.2007.03>

Fayon, A., Tikoff, B., Kahn, M., & Gaschnig, R. (2017). Cooling and exhumation of the southern Idaho batholith. *Lithosphere*, 9, 299–314.

Ferns, M. L., & Brooks, H. (1995). The Bourne and Greenhorn subterrains of the Baker Terrane, northeastern Oregon: Implications for the evolution of the Blue Mountains island-arc system. *Geology of the Blue Mountains region of Oregon, Idaho, and Washington: Petrology and tectonic evolution of Pre-Tertiary rocks of the Blue Mountains region: US Geological Survey Professional Paper, 1438*, 331–358.

Foster, D., Doughty, P., Kalakay, T., Fanning, C., Coyner, S., Grice, W., & Vogl, J. (2007). Kinematics and timing of exhumation of metamorphic core complexes along the Lewis and Clark fault zone, northern Rocky Mountains, USA. *Geological Society Of America - Special Paper*, 434, 207.

Foster, D. A., & Fanning, C. M. (1997). Geochronology of the northern Idaho batholith and the Bitterroot metamorphic core complex: Magmatism preceding and contemporaneous with extension. *Geological Society of America Bulletin*, 109(4), 379–394. [https://doi.org/10.1130/0016-7606\(1997\)109<0379:GOTNIB>2.3.CO;2](https://doi.org/10.1130/0016-7606(1997)109<0379:GOTNIB>2.3.CO;2)

Foster, D., Grice, W., & Kalakay, T. (2010). Extension of the Anaconda metamorphic core complex: 40Ar/39Ar thermochronology and implications for Eocene tectonics of the northern Rocky Mountains and the Boulder batholith. *Lithosphere*, 2(4), 232–246.

Foster, D. A., Mueller, P. A., Mogk, D. W., Wooden, J. L., & Vogl, J. J. (2006). Proterozoic evolution of the western margin of the Wyoming craton: implications for the tectonic and magmatic evolution of the northern Rocky Mountains. *Canadian Journal of Earth Sciences*, 43(10), 1601–1619. <https://doi.org/10.1139/E06-052>

Foster, D. A., Schafer, C., Fanning, C. M., & Hyndman, D. W. (2001). Relationships between crustal partial melting, plutonism, orogeny, and exhumation: Idaho–Bitterroot batholith. *Tectonophysics*, 342(3–4), 313–350. [https://doi.org/10.1016/S0040-1951\(01\)00169-X](https://doi.org/10.1016/S0040-1951(01)00169-X)

Gallego, A., Russo, R., Comte, D., Mocanu, V., Murdie, R., & Vandecar, J. (2010). Seismic noise tomography in the Chile ridge subduction region. *Geophysical Journal International*, 182(3), 1478–1492. <https://doi.org/10.1111/j.1365-246x.2010.04691.x>

Gaschnig, R., Vervoort, J., Lewis, R., & McClelland, W. (2010). Migrating magmatism in the northern US Cordillera: in situ U–Pb geochronology of the Idaho batholith. *Contributions to Mineralogy and Petrology*, 159(6), 863–883. <https://doi.org/10.1007/s00410-009-0459-5>

Gaschnig, R., Vervoort, J., Lewis, R., & Tikoff, B. (2011). Isotopic evolution of the Idaho batholith and Challis intrusive province, northern US Cordillera. *Journal of Petrology*, 52(12), 2397–2429. <https://doi.org/10.1093/petrology/egr050>

Gaschnig, R. M., Vervoort, J. D., Lewis, R. S., & Tikoff, B. (2013). Probing for Proterozoic and Archean crust in the northern U.S. Cordillera with inherited zircon from the Idaho batholith. *Geological Society of America Bulletin*, 125(1–2), 73–88. <https://doi.org/10.1130/B30583.1>

Gerstoft, P., Sabra, K., Roux, P., Kuperman, W., & Fehler, M. (2006). Green's functions extraction and surface-wave tomography from microseisms in Southern California. *Geophysics*, 71(4), SI23–SI31.

Giorgis, S., McClelland, W., Fayon, A., Singer, B. S., & Tikoff, B. (2008). Timing of deformation and exhumation in the western Idaho shear zone, McCall, Idaho. *Geological Society of America Bulletin*, 120(9–10), 1119–1133.

Goldstein, P. (2003). Sac2000: Signal processing and analysis tools for seismologists and engineers, *The IASPEI International Handbook of Earthquake and Engineering Seismology, chapter 85* (pp. 1613–1614). London: Academic Press.

Goldstein, P., & Snoke, A. (2005). SAC availability for the IRIS community. *Incorporated Institutions for Seismology Data Management Center Electronic Newsletter*. Retrieved from <http://www.iris.edu/dms/newsletter/vol7/no1/sac-availability-for-the-iris-community/>

Gray, K. D., & Oldow, J. S. (2005). Contrasting structural histories of the Salmon River belt and Wallowa terrane: Implications for terrane accretion in northeastern Oregon and west-central Idaho. *Geological Society of America Bulletin*, 117(5–6), 687–706. <https://doi.org/10.1130/B25411.1>

Henstock, T. J., Levander, A., Snelson, C. M., Keller, G. R., Miller, K. C., Harder, S. H., et al. (1998). Probing the Archean and Proterozoic lithosphere of western North America. *GSA Today*, 8(7), 1–5.

Herrmann, R. B. (2013). *Computer programs in seismology*. Seismological Research Letters: An evolving tool for instruction and research. <https://doi.org/10.1785/0220110096>

Hoffman, P. F. (1988). United plates of America, the birth of a craton: Early Proterozoic assembly and growth of Laurentia. *Annual Review of Earth and Planetary Sciences*, 16(1), 543–603.

- Holbrook, S. W., Lizarralde, D., McGeary, S., Bangs, N., & Diebold, J. (1999). Structure and composition of the Aleutian island arc and implications for continental crustal growth. *Geology*, 27(1), 31–34. [https://doi.org/10.1130/0091-7613\(1999\)027<0031:SACOTA>2.3.CO;2](https://doi.org/10.1130/0091-7613(1999)027<0031:SACOTA>2.3.CO;2)
- Housen, B. A., & Dorsey, R. J. (2005). Paleomagnetism and tectonic significance of Albian and Cenomanian Turbidites, Ochoco Basin, Mitchell Inlier, central Oregon. *Journal of Geophysical Research*, 110, B07102. <https://doi.org/10.1029/2004JB003458>
- Jordan, T. E., & Allmendinger, R. W. (1986). The Sierras Pampeanas of Argentina; a modern analogue of Rocky Mountain foreland deformation. *American Journal of Science*, 286(10), 737–764.
- Karlstrom, K., Bowring, S., Chamberlain, K., Dueker, K., Eshete, T., Erslev, E., et al. (2002). Structure and evolution of the lithosphere beneath the Rocky Mountains: Initial results from the CD-ROM experiment. *GSA today*, 12(3), 4–10.
- Kay, R. W., & Kay, S. M. (1993). Delamination and delamination magmatism. *Tectonophysics*, 219(1-3), 177–189. [https://doi.org/10.1016/0040-1951\(93\)90295-U](https://doi.org/10.1016/0040-1951(93)90295-U)
- Kern, H. (2011). Measuring and modeling of P- and S-wave velocities on crustal rocks: A key for the interpretation of seismic reflection and refraction data. <https://doi.org/10.1155/2011/530728>
- Kurz, G. A., Schmitz, M. D., Northrup, C. J., & Vallier, T. L. (2017). Isotopic compositions of intrusive rocks from the Wallowa and Olds ferry arc terranes of northeastern Oregon and western Idaho: Implications for Cordilleran evolution, lithospheric structure, and Miocene magmatism. *Lithosphere*, 9(2), 235–264. <https://doi.org/10.1130/L550.1>
- LaMaskin, T. A., & Dorsey, R. J. (2016). Westward growth of Laurentia by pre-Late Jurassic terrane accretion, eastern Oregon and western Idaho, United States: A reply. *The Journal of Geology*, 124(1), 143–147.
- LaMaskin, T. A., Dorsey, R. J., & Vervoort, J. D. (2008). Tectonic controls on mudrock geochemistry, mesozoic rocks of eastern Oregon and western Idaho, USA: Implications for Cordilleran tectonics. *Journal of Sedimentary Research*, 78(12), 765–783. <https://doi.org/10.2110/jsr.2008.087>
- LaMaskin, T. A., Dorsey, R. J., Vervoort, J. D., Schmitz, M. D., Tumpane, K. P., & Moore, N. O. (2015). Westward growth of Laurentia by pre-Late Jurassic terrane accretion, eastern Oregon and western Idaho, United States. *The Journal of Geology*. <https://doi.org/10.1086/681724>
- LaMaskin, T. A., Vervoort, J. D., Dorsey, R. J., & Wright, J. E. (2011). Early mesozoic paleogeography and tectonic evolution of the western United States: Insights from detrital zircon U-Pb geochronology, Blue Mountains province, northeastern Oregon. *Geological Society of America Bulletin*, 123(9-10), 1939–1965. <https://doi.org/10.1130/B30260.1>
- Lallemant, H. A. (1995). Pre-Cretaceous tectonic evolution of the Blue Mountains province, northeastern Oregon. *US Geological Survey Professional Paper*, 1438, 271–304.
- Lewis, R. S., & Kiilsgaard, T. H. (1991). Eocene plutonic rocks in south central Idaho. *Journal of Geophysical Research*, 96(B8), 13,295–13,311.
- Lin, F.-C., Moschetti, M. P., & Ritzwoller, M. H. (2008). Surface wave tomography of the western United States from ambient seismic noise: Rayleigh and Love wave phase velocity maps. *Geophysical Journal International*, 173(1), 281–298. <https://doi.org/10.1111/j.1365-246X.2008.03720.x>
- Lobkis, O., & Weaver, R. (2001). On the emergence of the Green's function in the correlations of a diffuse field. *The Journal of the Acoustical Society of America*, 110, 3011.
- Lombardi, D., Braunmiller, J., Kissling, E., & Giardini, D. (2008). Moho depth and Poisson's ratio in the western-central Alps from receiver functions. *Geophysical Journal International*, 173(1), 249–264. <https://doi.org/10.1111/j.1365-246X.2007.03706.x>
- Lund, K. (2008). Geometry of the Neoproterozoic and Paleozoic rift margin of western Laurentia: Implications for mineral deposit settings. *Geosphere*, 4(2), 429–444.
- Lund, K., Aleinikoff, J. N., Evans, K. V., & Fanning, C. M. (2003). SHRIMP U-Pb geochronology of Neoproterozoic Windermere Supergroup, central Idaho: Implications for rifting of western Laurentia and synchronicity of Sturtian glacial deposits. *Geological Society of America Bulletin*, 115(3), 349–372. [https://doi.org/10.1130/0016-7606\(2003\)115<0349:SUPGON>2.0.CO;2](https://doi.org/10.1130/0016-7606(2003)115<0349:SUPGON>2.0.CO;2)
- Lund, K., & Snee, L. (1988). Metamorphism, structural development, and age of the continent-island arc juncture in west-central Idaho. In W. G. Ernst (Ed.), *Metamorphism and Crustal Evolution of the Western Coterminous United States, Rubey volume VII* (pp. 296–331). Englewood Cliffs, NJ: Prentice Hall.
- McKay, M. P., Bollen, E. M., Gray, K. D., Stowell, H. H., & Schwartz, J. J. (2017). Prolonged metamorphism during long-lived terrane accretion: Sm-Nd garnet and U-Pb zircon geochronology and pressure-temperature paths from the Salmon River suture zone, west-central Idaho, USA. *Lithosphere*, 9(5), 683–701. <https://doi.org/10.1130/L642.1>
- Miller, C. F., & Bradfish, L. J. (1980). An inner Cordilleran belt of muscovite-bearing plutons. *Geology*, 8(9), 412–416.
- Miller, D. J., & Christensen, N. L. (1994). Seismic signature and geochemistry of an island arc: A multidisciplinary study of the Kohistan accreted terrane, northern Pakistan. *Journal of Geophysical Research*, 99(B6), 11,623–11,642.
- Mueller, P. A., Wooden, J. L., Mogk, D. W., & Foster, D. A. (2011). Paleoproterozoic evolution of the Farmington zone: Implications for terrane accretion in southwestern Laurentia. *Lithosphere*, 3(6), 401–408. <https://doi.org/10.1130/L161.1>
- Mullen, E. D. (1978). Geology of the Greenhorn Mountains, northeastern Oregon (Master's thesis), Oregon State University, Corvallis.
- Payne, S., McCaffrey, R., King, R., & Kattenhorn, S. (2012). A new interpretation of deformation rates in the Snake River Plain and adjacent basin and range regions based on GPS measurements. *Geophysical Journal International*, 189, 101–122.
- Price, R. A., & Sears, J. W. (2000). A preliminary palinspastic map of the Mesoproterozoic Belt-Purcell Supergroup, Canada and USA: Implications for the tectonic setting and structural evolution of the Purcell anticlinorium and the Sullivan deposit. *Mineral Deposits Division, Special Publication*, 1, 61–81.
- Pyle, L. J., & Barnes, C. R. (2003). Lower Paleozoic stratigraphic and biostratigraphic correlations in the Canadian Cordillera: Implications for the tectonic evolution of the Laurentian margin. *Canadian Journal of Earth Sciences*, 40(12), 1739–1753.
- Reidel, S. P., Camp, V. E., Tolan, T. L., Kauffman, J. D., & Garwood, D. L. (2013). Tectonic evolution of the Columbia River flood basalt province. *Geological Society of America Special Papers*, 497, 293–324. [https://doi.org/10.1130/2013.2497\(12\)](https://doi.org/10.1130/2013.2497(12))
- Ross, G. (1991). Tectonic setting of the Windermere Supergroup revisited. *Geology*, 19(11), 1125–1128.
- Russo, R., & Silver, P. (1996). Cordillera formation, mantle dynamics, and the Wilson cycle. *Geology*, 24(6), 511–514.
- Schwartz, J. J., Snoke, A. W., Cordey, F., Johnson, K., Frost, C. D., Barnes, C. G., et al. (2011). Late Jurassic magmatism, metamorphism, and deformation in the Blue Mountains province, northeast Oregon. *Geological Society of America Bulletin*, B30, 327–1. <https://doi.org/10.1130/B30327.1>
- Schwartz, J. J., Snoke, A. W., Frost, C. D., Barnes, C. G., Gromet, L. P., & Johnson, K. (2010). Analysis of the Wallowa-Baker terrane boundary: Implications for tectonic accretion in the Blue Mountains province, northeastern Oregon. *Geological Society of America Bulletin*, 122(3-4), 517–536. <https://doi.org/10.1130/B26493.1>
- Selverstone, J., Wernicke, B. P., & Aliberti, E. A. (1992). Intracontinental subduction and hinged unroofing along the Salmon River suture zone, west central Idaho. *Tectonics*, 11(1), 124–144.

- Sewall, J. O., & Fricke, H. C. (2013). Andean-scale highlands in the late Cretaceous Cordillera of the north American western margin. *Earth and Planetary Science Letters*, 362, 88–98.
- Shapiro, N., & Campillo, M. (2004). Emergence of broadband Rayleigh waves from correlations of the ambient seismic noise. *Geophysical Research Letters*, 31, L07614. <https://doi.org/10.1029/2004GL019491>
- Shapiro, N., Campillo, M., Stehly, L., & Ritzwoller, M. (2005). High-resolution surface-wave tomography from ambient seismic noise. *Science*, 307(5715), 1615–1618.
- Shapiro, N., & Ritzwoller, M. (2002). Monte-Carlo inversion for a global shear-velocity model of the crust and upper mantle. *Geophysical Journal International*, 151(1), 88–105.
- Shillington, D. J., Van Avendonk, H. J., Holbrook, W. S., Kelemen, P. B., & Hornbach, M. J. (2004). Composition and structure of the central Aleutian island arc from arc-parallel wide-angle seismic data. *Geochemistry, Geophysics, Geosystems*, 5, Q10006. <https://doi.org/10.1029/2004GC000715>
- Sims, P. K., Lund, K., & Anderson, E. (2005). Precambrian crystalline basement map of Idaho—An interpretation of aeromagnetic anomalies. USGS Numbered Series 2884, USGS.
- Stanciu, A. C. (2015). Seismic investigations of the Earth's lithosphere and asthenosphere in two unique convergent margin settings (PhD thesis), University of Florida. Retrieved from <http://ufdc.ufl.edu/ufetd>
- Stanciu, A., Russo, R., Mocanu, V., Bremner, P., Hongsresawat, S., Torpey, M., et al. (2016). Crustal structure beneath the blue mountains terranes and cratonic north America, eastern Oregon, and Idaho, from teleseismic receiver functions. *Journal of Geophysical Research: Solid Earth*, 121, 5049–5067. <https://doi.org/10.1002/2016JB012989>
- Stewart, J. H. (1972). Initial deposits in the cordilleran geosyncline: Evidence of a late Precambrian (<850 m.y.) continental separation. *Geological Society of America Bulletin*, 83(5), 1345–1360.
- Strayer, L. M., Hyndman, D., Sears, J., & Myers, P. (1989). Direction and shear sense during suturing of the seven Devils-Wallowa terrane against North America in western Idaho. *Geology*, 17(11), 1025–1028.
- Suyehiro, K., Takahashi, N., Ariie, Y., Yokoi, Y., Hino, R., Shinohara, M., et al. (1996). Continental crust, crustal underplating, and low-Q upper mantle beneath an oceanic island arc. *Science*, 272(5260), 390–392. <https://doi.org/10.1126/science.272.5260.390>
- Takahashi, N., Kodaira, S., Klemperer, S. L., Tatsumi, Y., Kaneda, Y., & Suyehiro, K. (2007). Crustal structure and evolution of the Mariana intra-oceanic island arc. *Geology*, 35(3), 203–206. <https://doi.org/10.1130/G23212A.1>
- Tarantola, A. (2005). *Inverse problem theory and methods for model parameter estimation*. siam.
- Tikoff, B., Kelso, P., Manduca, C., Markley, M., & Gillaspay, J. (2001). Lithospheric and crustal reactivation of an ancient plate boundary: The assembly and disassembly of the Salmon River suture zone, Idaho, USA. *Geological Society, London, Special Publications*, 186(1), 213–231.
- Tikoff, B., Vervoort, J., Hole, J., Russo, R., Gaschnig, R., & Fayon, A. (2017). Introduction: Earthscope IDOR project (deformation and magmatic modification of a steep continental margin, western Idaho–eastern Oregon) themed issue. *Lithosphere*, 9(2), 151–156. <https://doi.org/10.1130/L628.1>
- Tumpane, K. P. (2010). Age and isotopic investigations of the olds ferry terrane and its relations to other terranes of the Blue Mountains province, eastern Oregon and west-central Idaho (Master's thesis), Boise State University Thesis and Dissertations. Retrieved from <http://scholarworks.boisestate.edu/td/88>, paper 88.
- Vogl, J. J., Min, K., Carmenate, A., Foster, D. A., & Marsellos, A. (2014). Miocene regional hotspot-related uplift, exhumation, and extension north of the Snake River Plain: Evidence from apatite (U-Th)/He thermochronology. *Lithosphere*, 6(2), 108–123. <https://doi.org/10.1130/L308.1>
- Wessel, P., & Smith, W. H. (1998). New, improved version of generic mapping tools released. *Eos, Transactions American Geophysical Union*, 79(47), 579–579. <https://doi.org/10.1029/98EO00426>
- Wessel, P., Smith, W. H., Scharroo, R., Luis, J., & Wobbe, F. (2013). Generic mapping tools: Improved version released. *Eos, Transactions American Geophysical Union*, 94(45), 409–410. <https://doi.org/10.1002/2013EO450001>
- Winston, D., & Link, P. (1993). Middle Proterozoic rocks of Montana, Idaho, and Washington: The Belt Supergroup. *Precambrian of the Conterminous United States: Boulder, Colorado, Geological Society of America, The Geology of North America, C-3*, 487–521.
- Wylde, S. J., & Wright, J. E. (2001). New evidence for Cretaceous strike-slip faulting in the United States Cordillera and implications for terrane-displacement, deformation patterns, and plutonism. *American Journal of Science*, 301(2), 150–181. <https://doi.org/10.2475/ajs.301.2.150>
- Yang, Y., Shen, W., & Ritzwoller, M. (2011). Surface wave tomography on a large-scale seismic array combining ambient noise and teleseismic earthquake data. *Earthquake Science*, 24(1), 55–64.
- Zhu, L., & Kanamori, H. (2000). Moho depth variation in Southern California from teleseismic receiver functions. *Journal of Geophysical Research*, 105(B2), 2969–2980. <https://doi.org/10.1029/1999JB900322>